NAM

Improving the Functional and Stochastic Model of In-SAR

F.J. van Leijen, S. Samiei-Esfahany, H. van der Marel and R.F. Hanssen

Delft University of Technology

Datum April 2020

Editors Jan van Elk & Dirk Doornhof

General Introduction

Gas production and the resulting reduction of reservoir pressure cause compaction of the reservoir formation. This is expressed as subsidence at surface, which e.g. requires measures to maintain the ground water level in the area above the Groningen gas field. Subsidence measurements are also used to determine the compaction of the gas reservoir, which drives seismicity in the Groningen area. Monitoring of subsidence is therefore an important activity for NAM. Different techniques are used to monitor subsidence: levelling surveys, GPS-measurements and InSAR satellite observations. It is essential to obtain a realistic description of the uncertainties in the geodetic measurements, to be able to interpret the subsidence signal, and to perform subsurface and geomechanical modelling in an objective way.

The Study and Data Acquisition Plan for Winningsplan 2016 (ref. 1 and 2) included a research program into the monitoring of subsidence aiming to improve the processing and interpretation of the GNSS (Ref. 3 and 4) and In-SAR technologies (Ref. 5 and 6). The stochastic modelling of levelling and GNSS were studied earlier (Ref. 8). The current study addresses stochastic modelling for the In-SAR technique.

There are two main improvement areas for the stochastic modelling of InSAR data:

1. Handling large data dimensions: a computational efficient method is required that results in a full covariance matrix in which off-diagonal elements are not neglected.
2. Minimization of potential biases in the stochastic model due to choices made on the functional model (e.g., modelling InSAR time series as a linear deformation rate).

The objective of this study was to develop and evaluate algorithms to improve InSAR data analysis. Since the functional and stochastic modelling of the InSAR observations influence each other, both aspects were studied.

This study has resulted in a pragmatic approach to obtain an InSAR stochastic model that can handle large data dimensions, and reduces the effect of functional modelling.

Different data reduction techniques can be applied to generate a spatially reduced dataset, such as the use of a regular grid, a quadtree decomposition, clustering techniques such as K-means, and a reduction to existing benchmark locations. The latter is especially relevant regarding the integration with other geodetic techniques, such as levelling and Global Navigation Satellite Systems (GNSS).

A standardized InSAR data format is proposed, that can be used both for original InSAR datasets of individual scatterers, as well as for reduced datasets. The data format is based on the space-time matrix concept, that enables the storage of InSAR observations in undifferenced format, together with information on points and epochs.

To reduce potential biases in the stochastic model due to choices in the functional model, two studies are performed. The added value of the use of Numerical Weather Models (NWM) to mitigate the atmospheric signal delay is investigated. The analysis shows that no significant improvement, and even a slight deterioration, of the variability in the PS deformation time series is obtained when using NWM.

To optimize the fit of the functional models applied to the InSAR time series, three alternative approaches of Multiple Hypothesis Testing (MHT) have been implemented and evaluated.

Summarizing, the study ‘Improving the Functional and Stochastic Model of InSAR’ has delivered a pragmatic method for the computation of a full covariance matrix for (reduced) InSAR datasets, ready to be able to discriminate the deformation model(s) that best fit the geodetic data, and to integrate geodetic techniques (levelling, GNSS, InSAR) in the computation of subsidence signals.

References

1. Study and Data Acquisition Plan – Winningsplan 2016, NAM, Jan van Elk and Dirk Doornhof, April 2016
2. Study and Data Acquisition Plan update 2019, NAM, Jan van Elk and Dirk Doornhof, January 2019
3. Comparison of GNSS Processing Methodologies for Subsidence Monitoring, NAM GNSS APM Project Report, Hans van der Marel, TU Delft, Apr 2020.
4. GNSS-Processing in context with the 'Study and Data Acquisition Plan' related to the Production plan 'Winningsplan' Groningen, K. Hoentjen and L. Huisman, Geo-Information Services Kadaster, Mar 2019.
5. High resolution InSAR in the Groningen area - 2018-2019 Advanced Services, Yuxiao Qin, Jacqueline Salzer, Hanno Maljaars and Pieter Bas Leezenberg, SkyGeo, Nov 2019.
6. Improving the Functional and Stochastic Model of In-SAR, NAM INSAR FM SM Project Report, F.J. van Leijen, S. Samiei-Esfahany, H. van der Marel and R.F. Hanssen, TU Delft, Apr 2020.
7. Ensemble Based Subsidence application to the Ameland gas field – long term subsidence study part two (LTS-II) continued study. Technical report, 2017, NAM, Assen, Netherlands.

NAM

Title	**Improving the Functional and Stochastic Model of In-SAR**	**Date**	April 2020
		Initiator	NAM
Autor(s)	F.J. van Leijen, S. Samiei-Esfahany, H. van der Marel and R.F. Hanssen	**Editors**	Jan van Elk Dirk Doornhof
Organisation	Delft University of Technology	**Organisation**	NAM
Place in the Study and Data Acquisition Plan	Study Theme: Reservoir Compaction Comment: Gas production and the resulting reduction of reservoir pressure cause compaction of the reservoir formation. This is expressed as subsidence at surface, which e.g. requires measures to maintain the ground water level in the area above the Groningen gas field. Subsidence measurements are also used to determine the compaction of the gas reservoir, which drives seismicity in the Groningen area. Monitoring of subsidence is therefore an important activity for NAM. Different techniques are used to monitor subsidence: levelling surveys, GPS-measurements and In-SAR satellite observations. Study and Data Acquisition Plan for Winningsplan 2016, included a research program into the monitoring of subsidence aiming to improve the processing and interpretation of the GNSS and In-SAR technologies. The stochastic modelling of levelling and GNSS were studied earlier. The current study addresses stochastic modelling for the In-SAR technique. The objective of this study is to develop and evaluate algorithms to improve InSAR data analysis including evaluation of uncertainties. Since the functional and stochastic modelling of the InSAR observations influence each other, both aspects are studied.		
Associated research	(1) Development of compaction models based on core measurements. (2) Inversion of subsidence to derive compaction estimates. (3) Seismological modelling.		
Used data	InSAR High-resolution radar image stacks		
Associated organisations			
Assurance	Internal.		

Delft University of Technology

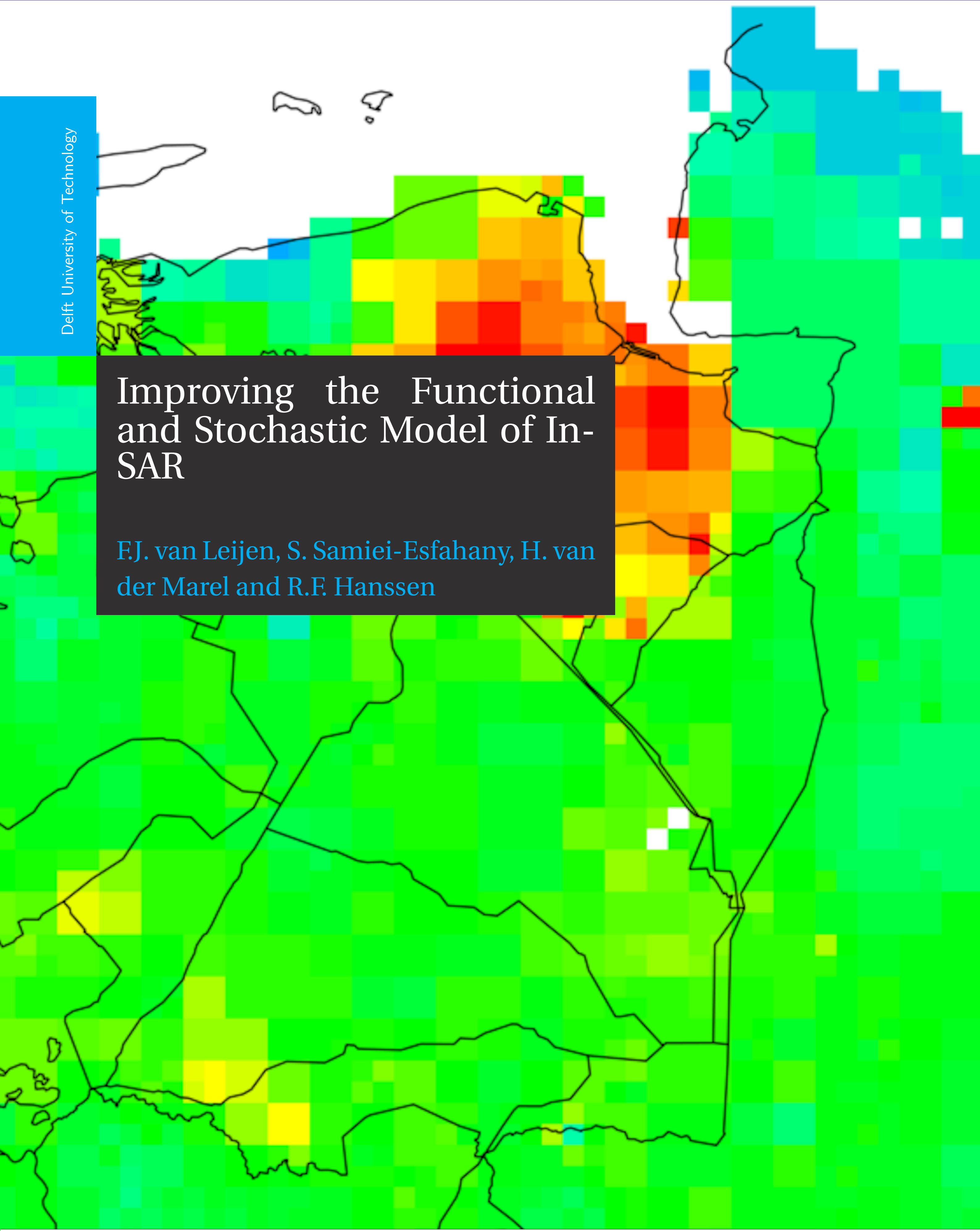

Improving the Functional and Stochastic Model of InSAR

F.J. van Leijen, S. Samiei-Esfahany, H. van der Marel and R.F. Hanssen

TU Delft
Delft
University of
Technology

Challenge the future

The front cover shows Sentinel-1 InSAR-based linear surface motion rates in the North of The Netherlands after spatial data reduction using a quadtree composition.

F.J. van Leijen, S. Samiei-Esfahany, H. van der Marel and R.F. Hanssen

Improving the Functional and Stochastic Model of InSAR

NAM INSAR FM SM Project Report

28 April 2020

Final report for the Nederlandse Aardolie Maatschappij (NAM), Improving the Functional and Stochastic model of geodetic techniques - InSAR project, Geodetic Studies TU Delft 2018/2019 (WO/NT No: 60301048 0020).

Publisher:

Faculty of Civil Engineering and Geosciences

Delft University of Technology

P.O. Box 5048

Stevinweg 1

2628 CN Delft

The Netherlands

The text has been type set using the MikTex 2.9 implementation of LaTeX. Graphs and diagrams were produced, if not mentioned otherwise, with Matlab.

CONTENTS

1

INTRODUCTION

This document reports on the study ‘Improving the Functional and Stochastic Model of InSAR’. This project has been carried out as part of the subsidence data acquisition scope from the ‘Study and Data Acquisition Plan Induced Seismicity in Groningen - Winningsplan 2016’. One of the geodetic studies included was supplemental research on the stochastic model of geodetic techniques. Since the stochastic model of leveling and GNSS has been addressed extensively in the Long Term Subsidence study project (NAM, 2017), the study reported in this document restricts to the InSAR technique.

It is essential to obtain a realistic description of the uncertainties in the geodetic measurements, to be able to interpret the subsidence signal, and to perform subsurface and geomechanical modeling in an objective way. Although scientific advances have been made on the InSAR stochastic model (see, e.g., Samiei-Esfahany (2017)), there are two main improvement areas:

1. Handling large data dimensions: a computational efficient method is required that results in a full covariance matrix in which off-diagonal elements are not neglected.
2. Minimization of potential biases in the stochastic model due to choices made on the functional model (e.g., modeling InSAR time series with a linear deformation rate only).

The objective of this study is to develop and evaluate algorithms to improve InSAR data analysis. Since the functional and stochastic modeling of the InSAR observations influence each other, both aspects are studied. The following research activities can be distinguished:

- An assessment of the effect of the use of Numerical Weather Models (NWM) for the mitigation of atmospheric signal delays (Chap. 2).
- The development of different InSAR data reduction methodologies (Chap.3).
- The development and evaluation of a pragmatic approach to obtain an InSAR stochastic model for reduced InSAR datasets (Chap. 4).
- The development and evaluation of hypothesis testing methodologies for the identification of the optimal functional model for InSAR time series (Chap. 5).
- The development of an InSAR standardized data format (NetCDF), for addition of the InSAR deformation estimates in the CUPiDO package that prepares geodetic measurements in double-difference (space-time) format including the covariance matrix, for confrontation against deformation models (Chap. 6).

The outcomes of this study are described in the chapters mentioned. A general conclusion is provided in Chap. 7.

2

MITIGATION OF ATMOSPHERIC SIGNAL DELAY

2.1. INTRODUCTION

One of the largest error sources in satellite radar interferometry (InSAR) is the atmospheric signal delay. Both the ionosphere and the troposphere contribute to the delay[1]. Since InSAR is only sensitive to the double-difference signal delay between acquisitions in time and between reflection points in space, not the size of the absolute delay, but the amount of spatial variability of the delays is of importance. This amount of spatial variability due the the ionosphere is relatively low, especially for radar systems with a short wavelength (e.g., X- or C-band). On the other hand, the spatial variability in the tropospheric signal delay can be large (Hanssen, 2001). Two delay-effects can be distinguished:

- Hydrostatic delay, which is dependent on the temperature and pressure distribution in the troposphere. Since the spatial variations of these quantities are typically rather smooth at a certain epoch, the differential delay in case of flat terrain is also relatively smooth. However, in case of large topographic height differences, the difference in tropospheric layering between the acquisitions causes a topography-related delay effect.
- Wet delay, primarily caused by the water vapor distribution in the troposphere. This distribution is strongly affected by turbulent processes and therefore highly variable.

Traditionally, the atmospheric signal delay in radar interferometric time series analysis, that is, the sum of the ionospheric and tropospheric signal delay, is estimated from the interferometric data stack itself (Ferretti et al., 2001, van Leijen, 2014). Hereby, the assumption is made that the signal delay is uncorrelated in time, but correlated in space. A sequential low-pass filter in time and a high-pass filter in space is applied to obtain an estimate of the atmospheric signal delay per acquisition. In addition, a height-dependent scaling factor can be estimated to account for the topography-related hydrostatic signal delay.

To improve the signal delay estimates, various approaches using auxiliary data have been evaluated. For example, the ENVISAT satellite contained both a SAR and a multi-spectral (MERIS) sensor to acquire information on the atmospheric signal delay simultaneously. However, evaluation showed that only in 2% of the cases usable MERIS acquisitions were obtained due to cloud cover and the need for acquisition during daytime (Liu, 2012). Alternatively, Numerical Weather Models (NWM) can be used. Various studies (Bekaert et al., 2015, Liu, 2012) showed that the temperature and pressure distribution can be modelled sufficiently well to reduce the hydrostatic delay effect in the InSAR data. This shows particularly in mountainous areas. However, the turbulent effect is much harder to model, both due to the limited spatial resolution of the models, and the sensitivity to the timing of the model runs. Typically, the NWM outcomes are generated at standard epochs, e.g., at 0h, 6h, 12h and 18h. Hence, the timing of the SAR acquisition will not be matching. But even if dedicated NWM products are generated at the exact times of SAR acquisitions, the uncertainty in e.g. the modeled wind fields will affect the distribution of the water vapor. E.g., a rain cloud, and the corresponding peak in water vapor distribution, can easily be a few kilometers off between the model and the true situation.

---

[1] The ionosphere is the layer 70 to 1000 km above the Earth's surface, the troposphere ranges from the surface to an altitude of 11-16 km.

To obtain better insight in the added value of the use of NWM in PSI time series analysis, a comparative analysis of different atmospheric mitigation approaches is performed. The methodologies applied are discussed in the next section.

2.2. METHODOLOGY

To assess the effect of the use of Numerical Weather Model (NWM) data in the PSI processing, a Sentinel-1 descending data stack is analyzed. The data (Track 37) covers the North of the Netherlands. The 133 images used span the period between November 2015 and October 2018. NWM realizations provided by the European Centre for Medium-Range Weather Forecasts (ECMWF) are used. Four PSI datasets are generated, based on different procedures to mitigate the atmospheric signal delay:

1. **Conventional approach**. The traditional methodology is applied, estimating the atmospheric delay from the radar data stack (Ferretti et al., 2001, van Leijen, 2014). Hereby, a low-pass Gaussian filter is applied to each time series to separate unmodeled deformation from the atmospheric signal delays. A Gaussian filter based on a standard deviation of $90/\sqrt{2}$ days is applied. The temporal filtering is followed by a spatial interpolation and smoothing based on Kriging. Hereby, for each acquisition a variogram is estimated to describe the spatial variability of the atmospheric signal delay.
2. **No atmosphere mitigation**. The atmospheric signal delay is not mitigated and remains in the final PSI results. Since a strict analysis without atmosphere mitigation does not result in a converging first-order network solution, a remove-compute-restore approach is applied. That is, the atmosphere is actually estimated and removed using the conventional approach, which is added back to the PSI results to obtain the final dataset including the atmospheric signal delay.
3. **ECMWF correction + conventional approach**. The ECMWF-based tropospheric signal delay is removed deterministically from the original phase observations. After this step, the conventional approach for atmosphere mitigation is applied.
4. **ECMWF correction only**. The ECMWF-based tropospheric signal delay is removed deterministically from the original phase observations, and no additional mitigation steps are applied.

The ECMWF-based tropospheric signal delays used are obtained using the GACOS service (Yu et al., 2018, 2017). This online service actually combines ECMWF HRES weather model data and Global Navigation Satellite System (GNSS)-based tropospheric delay estimates at nearby stations. The zenith delays provided by the GACOS service are mapped to the slant direction by division by the cosine of the local incidence angle.

Apart from the different approaches to mitigate the atmospheric signal delay, all other processing settings are kept equal. The final selection of detected PS is based on a ensemble coherence threshold of 0.7.

2.3. RESULTS

The estimated deformation rates obtained by the four different atmosphere mitigation approaches are shown in Figure 2.1. To minimize any potential offset between the references of the individual datasets, the reference is set to the mean deformation rate of each dataset based on the common PS among the sets (563062 PS).

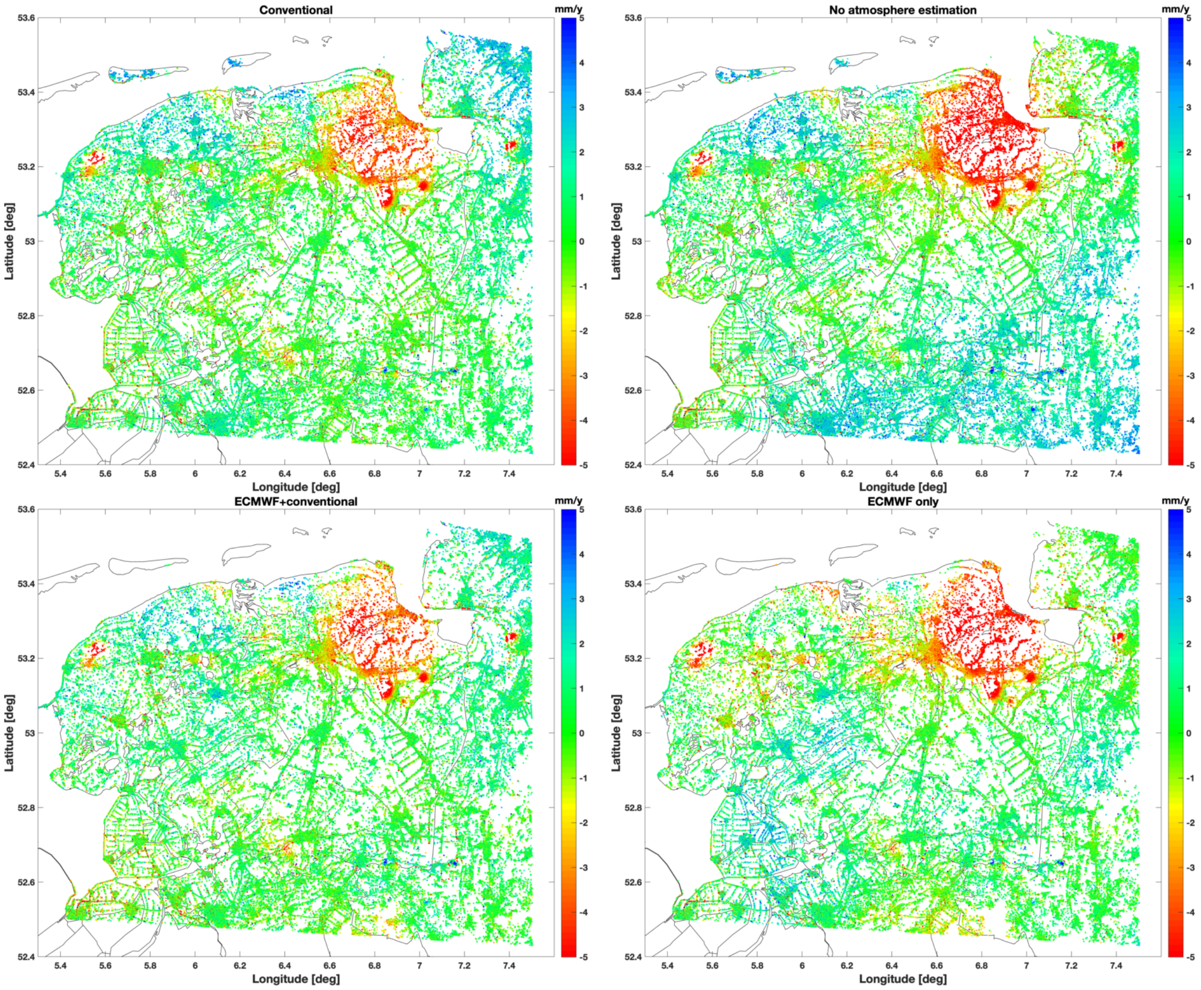

Figure 2.1: Linear deformation rates in the North of The Netherlands based on Sentinel-1 data (Track 37, November 2015 - October 2018), using four different approaches to mitigate the atmospheric signal delay.

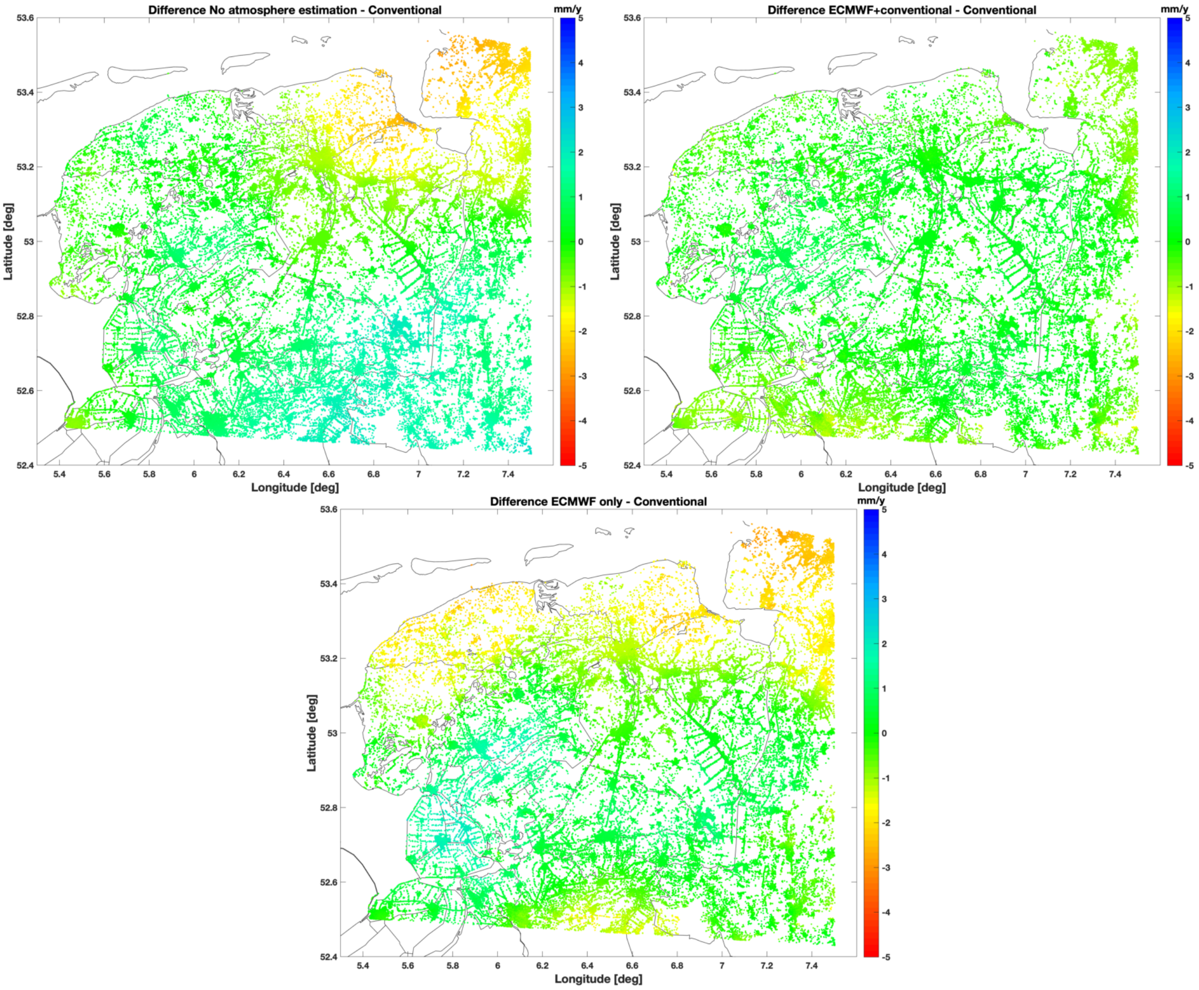

Figure 2.2: Difference in linear deformation rate between the alternative approaches and the conventional approach.

The results show differences in deformation rates, and, for example, that in some cases no PS are detected on the islands in the North. To obtain a better view on the discrepancies, Figure 2.2 contains the differences of the alternative approaches with respect to the conventional result. The difference with the ECMWF+conventional approach is minimal. However, for the other approaches the difference is significant.

To get a quantitative indication of the impact of the atmosphere mitigation approach, an assessment of the variation in the estimated deformation time series is made. Hereby, a linear deformation model is applied, and for each PS the RMSE of the residuals is calculated. The distribution of these RMSE-values is shown in Figure 2.3. The median and mean values are given in Table 2.1.

The plot shows the large variation in the time series in case no atmospheric mitigation is applied. With a deterministic correction by the ECMWF the RMSE in the time series drops to 9 mm. However, this is still significantly larger than the 3 mm RSME for the approaches involving the conventional approach. It should be noted that these relatively low values may be partly caused by the filtering applied in the conventional ap-

Table 2.1: Median and mean RMSE values of the residuals with respect to a linear deformation model for the different approaches.

Approach	Median RMSE [mm]	Mean RMSE [mm]
Conventional	2.7	2.8
No atmosphere	12.7	13.5
ECMWF+conventional	3.0	3.1
ECMWF only	9.0	9.4

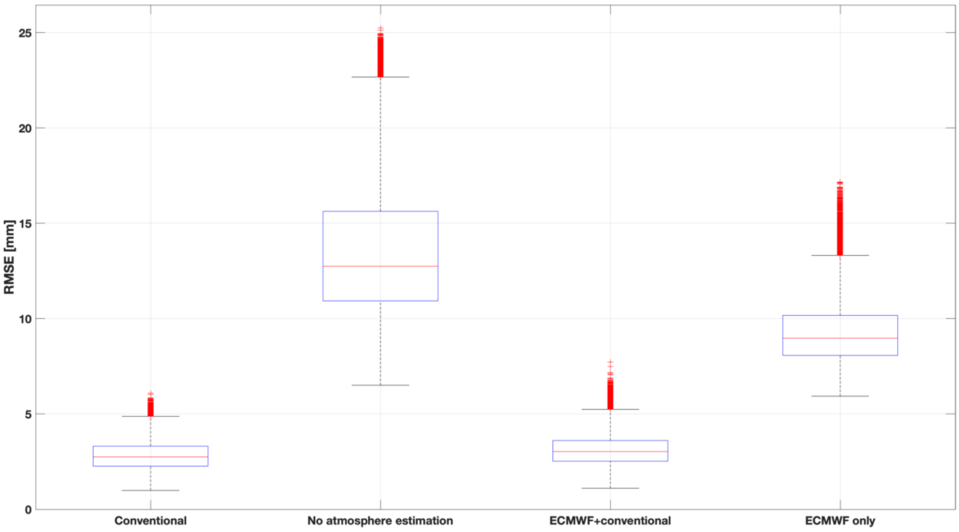

Figure 2.3: Boxplot of the RMSE values of the common PS residuals with respect to a linear model. The central red line indicates the median of the distribution, and the bottom and top edges of the blue box the 25th and 75th percentiles. The black whiskers extend to the most extreme values not considered to be outliers (within ± 2.7σ, assuming a normal distribution of the RMSE values (which is not the case for the positive-only RMSE values)). The outliers in the RMSE values are indicated with a red plus marker.

proach, which is also based on the residuals with respect to the deformation models used, which includes the linear model. Hence, this evaluation is not completely unbiased. However, it does shown that a deterministic correction only is not sufficient. The conventional and conventional+ECMWF approach only show a minimal difference in the RMSE.

2.4. CONCLUSIONS

The comparison of four different atmospheric signal delay mitigation approaches shows no significant improvement, and even a slight deterioration, of the variability in the PS deformation time series when using a ECMWF weather model. Although the evaluation method, based on the RMSE of residuals with respect to a linear deformation model, may be biased, the results do not indicate that the use of a weather model is beneficial. It should be noted that these results are only based on one case study, for a rather small area, and over a relatively flat terrain. Earlier studies showed that in case of large topographic height differences, where the vertical stratification effect is a more dominant contributor, the use of weather model data does in general result in an improvement. Hence, more case studies, for larger areas, and especially over flat terrain, should be performed to obtain a more representative assessment.

In any case, the error induced by the difference in timing between the NWM output generation and the SAR acquisition should be minimized. This timing effect has two causes: 1) the standardized output times of generic NWM results, and 2) the uncertainty in the NWM model parameters (e.g., wind speed and direction), affecting the distribution of the water vapor predictions. To account for the first cause, dedicated NWM runs should be performed, with outputs which are at least closer aligned to the SAR acquisitions. To reduce the effect of the shifts caused by the uncertainty in the model parameters, a NWM-SAR matching approach should be developed, to enable a transformation of the NWM delay screen to the measured SAR delays.

Furthermore, the ionospheric delay should be better accounted for in the analysis. These delays can either be modelled, or can be estimated from the SAR data using split-band algorithms (Brcic et al., 2010, Gomba et al., 2016). Although the ionospheric signal delays are relatively smooth in space, especially for radar signals with a short or medium wavelength (X- or C-band), certainly for a model-only approach, these delays should be accounted for. Although the conventional approach is well capable of estimating these low-frequency signals, the benefit of the use of these ionospheric models or split-band estimates should be assessed.

3

INSAR DATA REDUCTION

3.1. INTRODUCTION

InSAR data analysis typically results in datasets of millions of Persistent Scatterers (PS) and/or Distributed Scatterers (DS). Moreover, with the launch of SAR satellite constellations instead of single satellites, also the repeat cycle of the observation epochs reduces, resulting in hundreds of epochs per dataset. The consequence of this wealth of data is that the data becomes more difficult to analyze, visualize and compare with other data.

These difficulties not only hold for the observations themselves, but also for the stochastic properties of the data. Since the time series of all scatterers are in principle correlated with each other, the proper description of the stochastic characteristics would form a covariance matrix of impossible size to handle. In practice, this is therefore never done. However, a proper use of the stochastic model is desirable. Not only for the analysis of the dataset itself, but also for the integration of InSAR data with other geodetic datasets, such as obtained by levelling or GNSS.

To enable a proper analysis and integration of InSAR data, including their stochastic properties, data reduction is needed, both in space and in time. The *temporal* sampling of InSAR measurements is typically much higher compared to conventional techniques, such as levelling and campaign GNSS measurements. Therefore, a relatively simple temporal binning approach can be applied based on a (un)weighted average (Samiei-Esfahany and Bähr, 2015). Data reduction in the *spatial* domain is more challenging. In the following, a number of methodologies are presented and applied for the spatial data reduction.

3.2. METHODOLOGY

Different methods can be applied to reduce the size of an irregularly sampled dataset in space, such as an InSAR dataset. Here, sub-sampling, the application of a regular grid, a quadtree decomposition, K-means clustering, and a reduction to benchmark locations is discussed.

Sub-sampling

The most simple form of data reduction is sub-sampling. Hereby, every *n*th point in the dataset is taken. Hereby, As such, the data distribution of points is reduced in a quasi-random manner. A drawback of this approach is that the information in the removed data points is simply lost, and cannot be used to decrease the noise level in the reduced dataset.

Regular grid

The distribution of points can also be reduced to a regular grid. Hereby, a certain grid size is chosen, which is a trade-off between the resulting data size and the level of detail that remains. The actual choice needs to depend on the application and on computational resources, but may typically vary between hundreds of meters and a few kilometers. Given the points within each grid cell, a representative value of the InSAR time series should be computed. Here, various choices can be made. For instance the median value for each time series epoch can be used, or the mean value, in unweighted or weighted form. In case of a weighted form, the noise level for each individual scatterer can be used. In addition, a pre-selection of scatterers can be used.

For instance, only scatterers from objects or ground level (classified based on estimated height or contextual information) can be used, depending on the application.

Quadtree grid

As an alternative to a regular grid, which does not take signal variability or point density into account, a quadtree decomposition can be applied. Here the grid size is locally variable, depending on a certain criterion. This criterion can be a minimal number of points per grid cell (i.e., only sub-divide a grid cell if the new sub-grids all have a minimal number of points), a maximum number of points per grid cell (i.e., sub-divide when a grid cell contains more that the maximum number set), a maximum variability of the deformation signal in the grid cell, or a combination thereof. The maximum variability of the deformation signal can be based on estimated parameters, such as the linear deformation rate, or on the variability of the time series per epoch within the grid cell (Samiei-Esfahany and Bähr, 2015). Apart from these thresholds, a maximum and minimum grid size should be set.

Once the quadtree grid is obtained, the representative InSAR time series per grid cell can be calculated using the same approaches as applicable for the regular grid, i.e., a weighted or unweighted mean, or the median, based on all points or a sub-set thereof.

K-means clustering

A different strategy is to use point cloud clustering techniques. A frequently used clustering technique is K-means. Here, a set of points is clustered in a pre-defined number of clusters based on the distance between the points in the datasets. The clustering is optimized, based on a certain distance metric, such as the Euclidean distance. The largest disadvantage of the conventional K-means approach is the need to pre-define the number of clusters. In case of clustering an InSAR dataset, a pre-defined number is not desirable. Therefore, the Hierarchical K-means clustering approach is an interesting alternative (Samiei-Esfahany and Bähr, 2015). Hereby, a similar iterative approach as applied in a quadtree decomposition is applied. Once a clustering is obtained, a representative deformation time series can be obtained using points within the cluster, using similar methods as for a regular or quadtree grid.

Benchmark locations

Although the grid or cluster methods provide an effective strategy to reduce a dataset, they do not use information regarding the location of benchmarks used by other techniques. Hence, although the InSAR dataset will be reduced in size, no direct link to the other datasets is obtained. For a direct integration with other techniques, a data reduction technique based on existing benchmarks is desirable. To establish such a connection, the InSAR points within a certain radius around each benchmark can be selected. The same techniques as applicable for the gridding and clustering approaches can be used to derive a representative deformation time series. Since benchmarks are typically assumed to be fixed to objects with a stable foundation, a preselection of InSAR points can be made based the height of the scatterers, to isolate scatterers originating from objects.

3.3. RESULTS

The methods described to reduce the size of InSAR datasets in space are applied to a Sentinel-1 dataset of the northern part of The Netherlands, acquired between November 2015 and October 2018, see Fig. 3.1. The figure shows the linear deformation rates of the original set of scatterers, a sub-set, a reduction to benchmark locations, a K-means clustering, a regular grid and a quadtree decomposition. The preferable method depends on the application. For instance, for an integration with other techniques, data reduction towards benchmarks used by other techniques is most useful.

3.4. CONCLUSIONS

Different data reduction techniques can be applied to generate a spatially reduced dataset, such as a the use of a regular grid, a quadtree decomposition, clustering techniques such as K-means, and a reduction to existing benchmark locations. The most suitable approach is dependent on the application foreseen. The approach

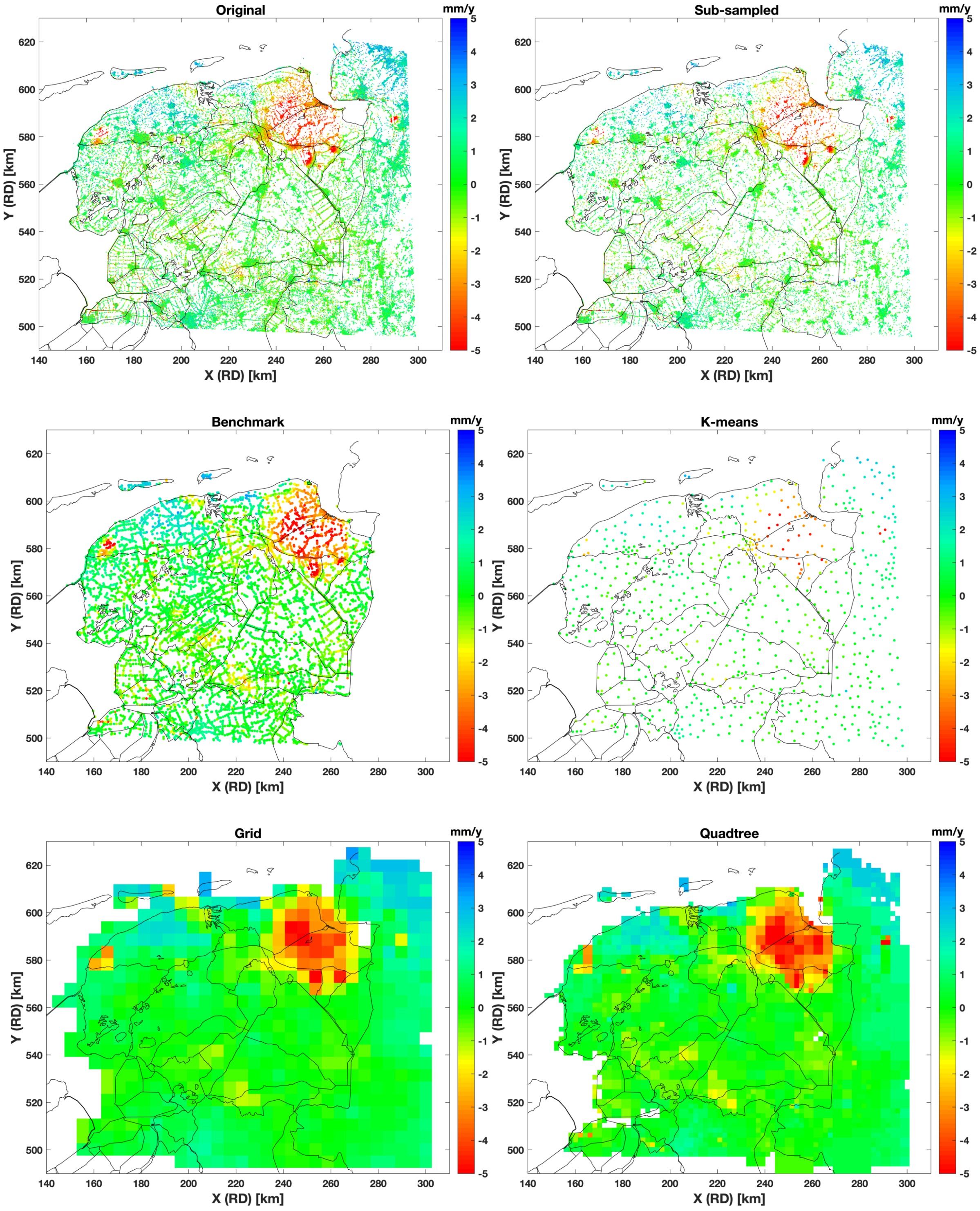

Original

Sub-sampled

Benchmark

K-means

Grid

Quadtree

Figure 3.1: Examples of spatial data reduction techniques, based on a Sentinel-1 dataset of the northern part of The Netherlands, acquired between November 2015 and October 2018. Examples show the result of sub-sampling (every 10th point), reduction to NAP benchmark locations in the area (unweighted mean of points within 500 meters of benchmark), K-means data reduction to 750 points (unweighted mean of points within cluster), a 5 km grid (unweighted mean of points) and a quadtree decomposition based on point density (minimal 100 points per grid cell, value based on unweighted mean).

based on benchmark locations is especially relevant regarding the integration with other geodetic techniques, such as levelling and Global Navigation Satellite Systems (GNSS). The reduced datasets are not only easier to analyze and visualize, but also enable the generation and application of the associated covariance matrix. The derivation of the full covariance matrix for reduced datasets is discussed in Chapter 4.

Apart from these advantages, it is important to consider that all data reduction approaches alter the original data, rely on assumptions of representativity, introduce artefacts by the applied methods, and effectively act as a low-pass filter. In other words, applying data reduction comes at a cost, the loss of potentially useful information.

4

STOCHASTIC MODEL FOR INSAR

4.1. BACKGROUND

Describing the precision of geodetic data in the form of the observations' second statistical moments or a noise covariance matrix, and using the inverse of the covariance matrix as a weight matrix in the estimation is common practice in geodesy and geophysical or geomechanical modeling. In particular for optimization problems that are based on the minimization of quadratic forms of errors (i.e., least squares estimation and L2-norm minimization), exploitation of the inverse of the covariance matrix as a weight matrix provides estimators with desired optimality aspects such as the minimum variance, and in case of Gaussian data, the maximum likelihood property. As a consequence, the correct description of observation noise, including its spatial and temporal correlation, is indispensable for stochastic modeling and construction of the covariance matrix of the observations.

The main objective of the stochastic modelling in this study is to describe the precision of InSAR data using a mathematical formulation. The main focus is on the second central moment of the noise, i.e., the covariance matrix. Note that InSAR datasets have a spatial as well as a temporal dimension, as they include deformation time series for a large set of persistent scatterers. The final goal is to propose an analytical formulation and a step-wise procedure to estimate the variances of all spatio-temporal deformation measurements and covariances among them, both for the original as well as for a derived dataset after data reduction, see Chap. 3.

Note that when we talk about stochastic modeling, we should acknowledge the difference between the so-called *measurement noise* and *idealization noise* components. Specifically, in deformation modeling, when identifying a deformation signal of interest (i.e., the unknown model parameters), any other deformation caused by other sources should be considered noise and their statistical properties should be described and included in the noise covariance matrix. In other words, in the context of deformation modeling, the term "noise" does not only comprise the uncertainty of the measurements itself (e.g., thermal noise, scattering noise, and atmospheric signal in InSAR) but it also absorbs all signal (or deformation) components in InSAR observations that are not identified as the signal of interest. Based on this definition, we encounter two different kinds of noise components. One is the random error of the measurements themselves, called *measurement noise*, while the other covers any other kind of deformation signal rather than the signal of interest. The latter is referred to as *idealization noise* (Baarda, 1976, Ketelaar, 2009, Samiei-Esfahany and Bähr, 2015).

We should note that the main objective of this study is to provide a stochastic model for the InSAR measurement noise only. In other words, the signal of interest here is defined as the total deformation (e.g., the summation of shallow and deep deformation signals), and consequently there is no idealization noise in the data. Although we acknowledge that the effect of the idealization noise components should be addressed functionally or stochastically in any geomechanical/geophysical modeling, the parametrization and modeling of these noise components for InSAR timeseries has not been investigated and discussed in this study.

While there are various studies in literature regarding noise characteristics in InSAR measurements (Agram and Simons, 2015, Hanssen, 2001), the effect of timeseries processing on the spatio-temporal variability of the noise components has been overlooked in the available InSAR stochastic models. Note that InSAR deformation estimates are affected by InSAR processing settings, in particular during the the spatio-temporal

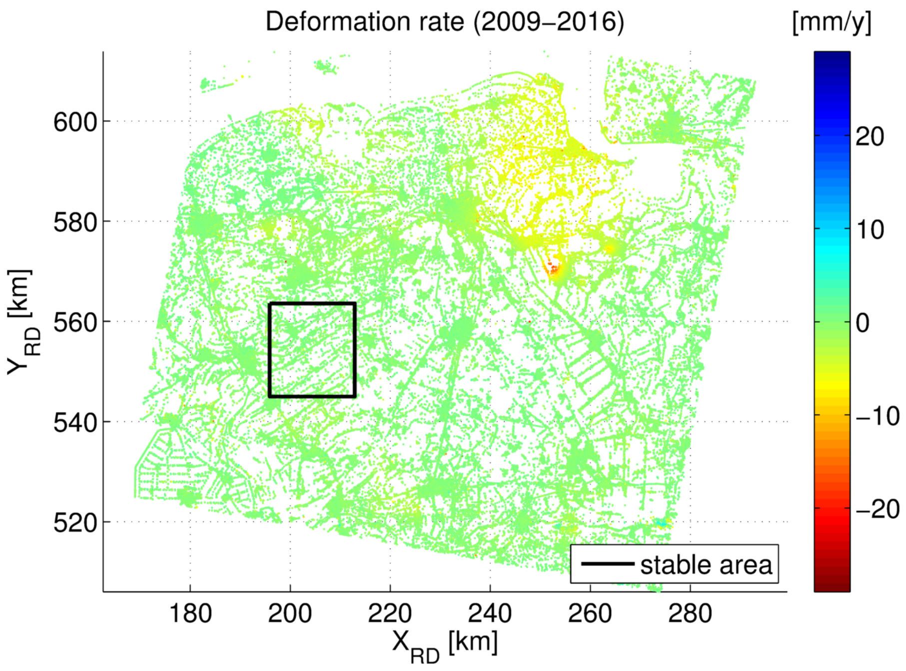

Figure 4.1: PSI velocity map of the Groningen area based on the RadarSAT-2 dataset acquired between September 2009 and November 2016. The black box shows the presumed signal-free area.

atmospheric filtering. In other words, the filtering of the atmospheric component inevitably alters the spatio-temporal noise structure of InSAR deformation estimates. As the filtering step and its setting may vary from case to case, it is difficult to derive a generic stochastic model for InSAR deformation timeseries.

In general, there are two ways of thinking regarding how to derive a spatio-temporal noise model for final InSAR timeseries. One is to derive or assume a noise structure for raw InSAR timeseries (before atmospheric filtering) followed by the design of an efficient error propagation scheme through all the processing steps. The other approach is to estimate the noise components directly from final InSAR timeseries over a presumably “signal-free” area. An example of the first approach and its difficulties has been demonstrated in (Samiei-Esfahany and Bähr, 2015). The challenges of this approach are i) that a reliable and generic initial noise structure is not always available, and ii) that the error prorogation through all the spatial and temporal steps of InSAR processing is too complex. Due to the limitations and complexities of the first approach, we have applied the second approach in this study. That is, we use InSAR data from a presumably stable area (signal-free area), and we subtract all the potential residual signals in order to isolate the effect of measurement noise components.

It should be noted that when we subtract a linear trend (i.e. the rate and the intercept) from data before variogram analysis, we in fact remove the effect of the master noise and master atmosphere from the InSAR observations. Moreover, if the spatial mean over the stable area is estimated and subtracted from the data before variogram analysis, the consequence is that the effect of the reference noise will be also removed. Therefore, we conclude that the proposed stochastic model describes the noise variability of undifferenced observations, and should be propagated further to derive the covariance matrix of double-difference observations, which is the common format of using InSAR data in geophysical and geomechanical modeling (see Chapter 6 for more information on undifferenced and double-differenced data).

4.2. STOCHASTIC MODELING: RADARSAT2 DATA

In order to evaluate the spatio-temporal variability of measurement noise, we analyzed an InSAR dataset over an presumably signal-free area close to the Groningen region. A RadarSAT2 dataset containing 97 radar images acquired between September 2009 and November 2016 was used for the study.

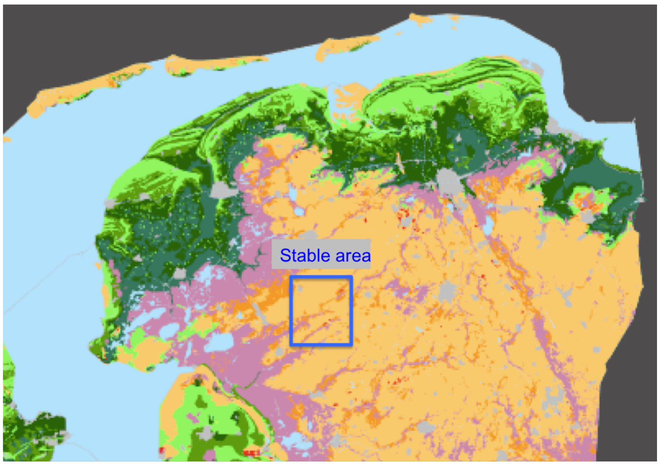

Figure 4.2: Soil map of the northern Netherlands and the selected presumably signal-free area.

Fig. 4.1 shows the selected study area (box of ~17×17 km) for the analysis. The assumption that it is unaffected by deep source subsidence is based on the absence of gas fields in the area. Also the velocity map of Fig. 4.1 shows that the PS points in the selected area have indeed low velocity. Another constraint was the absence of organic soils in the selected area. As we see in Fig. 4.2, the selected polygon covers limited peat areas and so the shallow deformation mechanisms are assumed to be minimal in the selected area.

In order to further reduce any residual signal in the dataset, a model containing a constant velocity and a sinusoidal signal with an annual period has been estimated and subtracted from each PS time series. Here, the main assumption is that if any residual signal (e.g. due to shallow deformation mechanisms or soil compaction) has remained in the data, it will follow a constant velocity plus a sinusoidal model. Thus, by correcting for these signals the residuals are assumed to contain only the effect of measurement noise in the data.

From the time series of the corrected observations in the selected area, the spatio-temporal empirical variograms are computed using robust algorithms (Cressie and Hawkins, 1980, Genton, 1998) in order to reduce the sensitivity to outliers. The empirical variograms are averaged per spatial and temporal bins. The results are visualized in Fig. 4.3.

Visual analysis of this figure shows the presence of both temporally and spatially correlated noise components in the InSAR dataset. We can recognize three different types of behavior in the spatio-temporal variograms: i) a nugget effect (~10mm^2), ii) a spatially 2nd order stationary correlated signal, and iii) a temporally correlated signal. To combine these three effects in a generic model, we can consider different kinds of spatio-temporal models. We tried four different models as follows:

1. Model with a nugget and a joint spatio-temporal exponential variogram function, with stationary behavior in both time and space:
$$\gamma(\Delta t, h) = \sigma_0^2 + \sigma_{st}^2 (1 - e^{\frac{-\Delta t}{R_t}} e^{\frac{-h}{R_s}}) \tag{4.1}$$
where Δt and h are the time difference between acquisitions and distance between PS points, respectively, σ_0^2 is the nugget, σ_{st}^2 is the variance of the joint spatio-temporal function, and R_t and R_s are the temporal and spatial range of the function.

2. Model with nugget and a joint spatio-temporal exponential variogram function, with non-stationary behavior in the time domain:
$$\gamma(\Delta t, h) = \sigma_0^2 + \sigma_{st}^2 \Delta t^{p_t} (1 - e^{\frac{-h}{R_s}}) \tag{4.2}$$
where p_t is the power of the non-stationary temporal behavior.

3. Model with nugget and distinct spatial and temporal variogram functions, with a non-stationary behavior in the time domain:
$$\gamma(\Delta t, h) = \sigma_0^2 + \sigma_t^2 \Delta T^{P_t} + \sigma_s^2 (1 - e^{\frac{-h}{R_s}}) \tag{4.3}$$

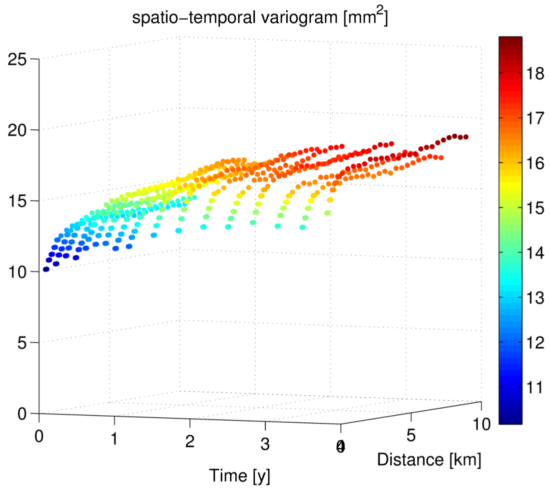

Figure 4.3: Empirical spatio-temporal variograms of RadarSAT2 InSAR data over the signal-free area.

where σ_s^2 and σ_t^2 are the variance of the spatial and the temporal functions, respectively.

4. Model with nugget and distinct spatial and temporal exponential variogram functions, with stationary behavior in both the space and time domain:

$$\gamma(\Delta t, h) = \sigma_0^2 + \sigma_t^2(1 - e^{\frac{-\Delta T}{R_t}}) + \sigma_s^2(1 - e^{\frac{-h}{R_s}}) \tag{4.4}$$

where σ_s^2 and σ_t^2 are the variance of the spatial and the temporal functions, respectively.

We used nonlinear weighted least squares to estimate the parameters of these four models to the emperical variograms. The weights are computed based on the number of variogram samples per bin. Table 4.1 shows the norm of the misfit (i.e., residuals) for the estimation of these four models. As the models have different numbers of parameters, we used the normalized norm (i.e. the norm divided by redundancy: $m-n$, where m and n are number of observations and unknowns, respectively) as the metric to evaluate which model has a better fit to the empirical variograms. Based on this analysis, generally distinct models (i.e., model 3 and 4) show better results. However, we cannot significantly distinct between model 3 and 4. As we do not have any physical explanation for the non-stationary signal in model 3, and also as the visual inspection of Figure 4.3 does not show significant non-stationary signal, we choose model 4 with stationary behavior in the time domain. Figs. 4.4 and 4.5 visualize the fitted model and Table 4.2 shows the estimated parameters of model 4.

Based on the obtained variogram model, the final covariance matrix of an InSAR spatio-temporal dataset can be constructed based on the summation of the three contributions (see Eq. (4.4)):

1. White noise or nugget (Q_n)
2. Temporally correlated component of noise (Q_t)
3. Spatially correlated component of noise (Q_s).

The final covariance matrix is then constructed as $Q = Q_n + Q_s + Q_t$. The components of the three covariance matrices (i.e., $\text{cov}\{y_i^{t_1}, y_j^{t_2}\}$ or the covariance between point i at time t_1 and point j at time t_2) are constructed based on the equations in Table 4.3.

4.3. ERROR PROPAGATION FOR REDUCED DATASETS

Using the model of Eq. (4.4) and Table 4.3, we can construct the full covariance matrix for an InSAR dataset. However, we should note that, due to large volumes of InSAR datasets (and consequently their large covari-

Table 4.1: Misfit and norm of the residuals for the four different variogram models, where $m = 568$ is the number of observations, n is the number of parameters of each model, e is the misfit vector and W is the weight matrix.

MODEL	number of parameters (n)	$e^T We$	$\frac{e^T We}{m-n}$
Model 1	4	495	0.88
Model 2	4	286	0.51
Model 3	5	130	0.23
Model 4	5	139	0.25

Table 4.2: Estimated parameters for the spatio-temporal variogram model of Eq. (4.4) for the RadarSAT2 dataset.

σ_0^2 [mm^2]	σ_t^2 [mm^2]	R_t [years]	σ_s^2 [mm^2]	R_s [km]
7.93	5.5	0.67	3.9	1.11

Table 4.3: How to compute $\text{cov}\{y_i^{t_1}, y_j^{t_2}\}$: the covariance between point i at time t_1 and point j at time t_2 for three contributing components of the final covariance matrix.

	Nugget effect [Q_n]	Temporal component [Q_t]	Spatial component [Q_s]
$i = j,\ t_1 = t_2$	σ_0^2	σ_t^2	σ_s^2
$i = j,\ t_1 \neq t_2$	0	$\sigma_t^2 e^{-\frac{\lvert\Delta t_{12}\rvert}{R_t}}$	0
$i \neq j,\ t_1 = t_2$	0	0	$\sigma_s^2 e^{-\frac{h_{ij}}{R_s}}$
$i \neq j,\ t_1 \neq t_2$	0	0	0

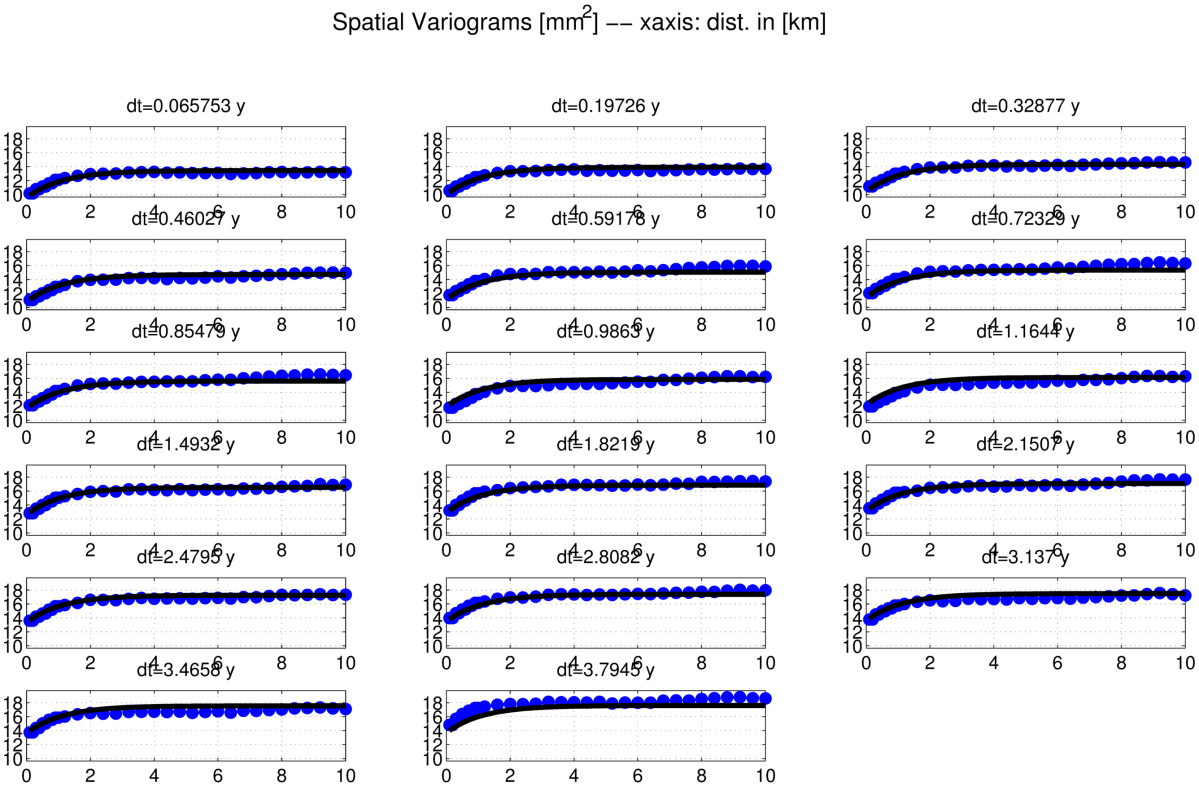

Figure 4.4: Fitted model to the spatial variogram profiles of RadarSAT2 InSAR data over the presumably signal-free area for different temporal lags (from 0.06 to 3.8 years). The horizontal axes are labeled by spatial lag in [m], and vertical axes display the variogram values in [mm^2].

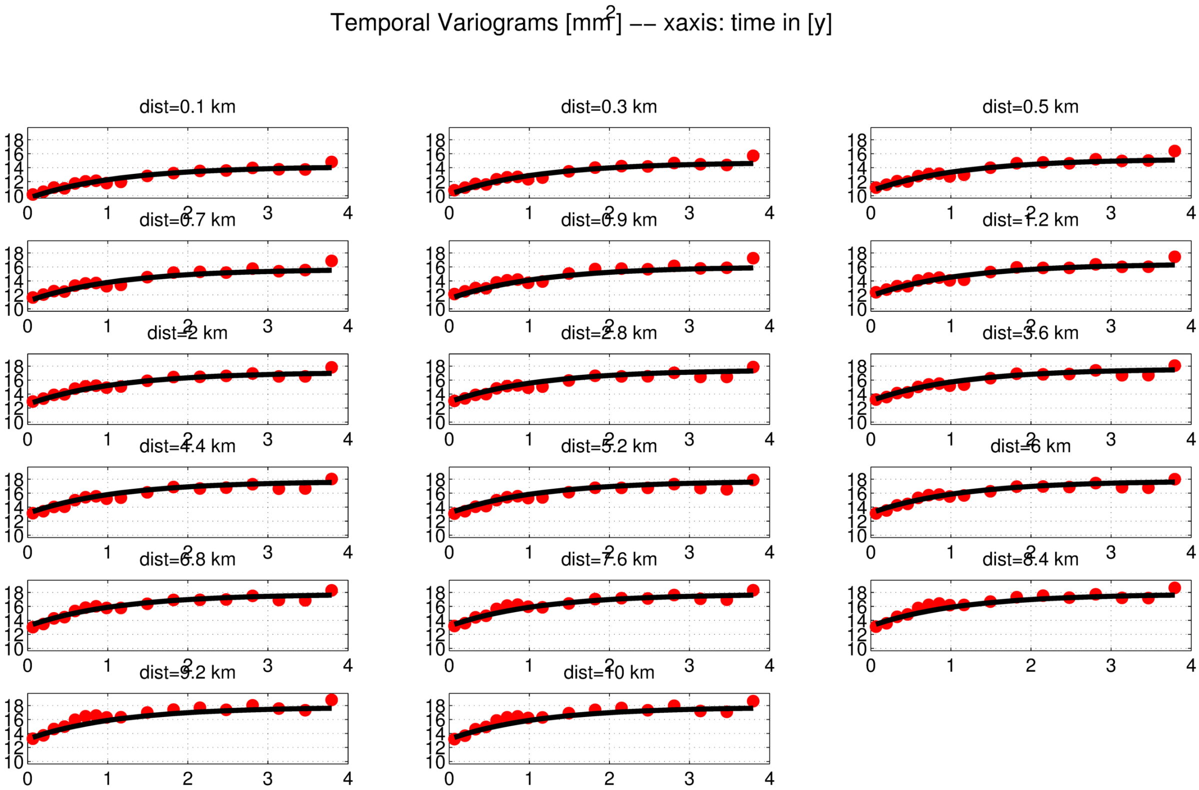

Figure 4.5: Fitted model to the temporal variogram profiles of RadarSAT2 InSAR data over the presumably signal-free area for different spatial lags (from 100 meter to 10 km). The horizontal axes are labeled by temporal lag in [years], and vertical axes display the variogram values in [mm^2].

ance matrices), an effective data reduction method is usually applied in practice on the data. Hence, in order to describe the quality of a reduced dataset, the covariance matrix of InSAR data should be propagated to the covariance matrix of the reduced dataset. For a data reduction method that can be formulated as a linear transformation (i.e., averaging in time and space as presented in Samiei-Esfahany and Bähr (2015)), a rigorous error propagation can be applied using the linear error propagation law. However, this approach imposes some practical limitations: it requires the construction of the huge covariance matrix of the initial dataset before the reduction, and so it requires high computational power. Also note that it is usually desirable not to store the full covariance matrix of the reduced dataset, but instead to have a covariance function that makes it possible to reconstruct the covariance elements afterwards (based on for example different settings of the applied reduction method). However, it is not possible to introduce a generic and exact covariance function for the reduced dataset as the number of points and distance among them is different for different averaging cells. Nevertheless, we may be able to approximate such a covariance model as a function of the number of points per averaging cell and also the average distance among points inside each cell. Hence, the main objective here is to derive a simple analytical equation for the elements of the covariance matrix of the reduced dataset. Note that we only consider averaging-based reduction methods, i.e. the methods that are based on (unweighted) averaging either in time, or in space, or in both. For simplicity, we first consider the error propagation for data reduction only in the space domain, and then we extend the formulation for the spatio-temporal data reduction.

Data reduction in the space domain

Let's assume that we have a spatial InSAR deformation dataset at only one epoch t_1. For data reduction, the points are clustered in different averaging cells, and the deformation of each cell is computed as the average of deformation of PSs within the cell. Note that, it is not the subject of this section to address how to define the number of cells and their shape and geometry. The cell structure can be defined based on different criteria and methods such as quadtree decomposition or K-means clustering (see Chapter 3 and Samiei-Esfahany and Bähr (2015)). Whatever method is used, the final deformation of an averaging cell is computed based on a simple averaging over the PS points in the associated cell. For an averaging cell with m number of PSs each with deformation y_i, the deformation vector and its covariance matrix can be written as

$$y = \begin{bmatrix} y_1 \\ y_2 \\ \vdots \\ y_m \end{bmatrix}, \quad Q_y = \begin{bmatrix} \sigma^2 & \sigma_{12} & \sigma_{13} & \dots & \sigma_{1m} \\ \sigma_{12} & \sigma^2 & \sigma_{23} & \dots & \sigma_{2m} \\ \vdots & \vdots & \vdots & \ddots & \vdots \\ \sigma_{1m} & \sigma_{2m} & \sigma_{3m} & \dots & \sigma^2 \end{bmatrix}, \tag{4.5}$$

where σ^2 is the variance and σ_{ij} is the covariance between points i and j. The values of σ^2 and σ_{ij} are computed based on a selected covariance model (for example the model in the third column of Table 4.3). Note that the fact that all the PS points have equal variance σ^2 is the inherent property of the covariance models that we assumed. Now, the deformation of the average in cell z and its variance σ_z^2 is computed as (see the appendix for the proof)

$$z = \frac{1}{m}\sum_{i=1}^{m} y_i, \quad \sigma_z^2 = \frac{\sigma^2 + (m-1)\bar{s}}{m}, \tag{4.6}$$

where $\bar{s}$ is the average of all the off-diagonal elements of Q_y:

$$\bar{s} = \frac{2}{m(m-1)} \sum_{i=1}^{m} \sum_{j=i+1}^{m} \sigma_{ij}. \tag{4.7}$$

Also, the covariance between two different spatial cells z_1 and z_2, with m_1 and m_2 number of PS in each cell and no overlaps between the cells, is given as (see the appendix for the proof)

$$\text{cov}\{z_1, z_2\} = \sigma_{z_1 z_2} = \frac{1}{m_1 m_2} \sum_{i=1}^{m_1} \sum_{j=1}^{m_2} c_{ij} = \bar{c}, \tag{4.8}$$

where $\bar{c}$ is the average of the c_{ij} elements that denote the elements of the cross-covariance between the points of the two cells:

$$Q_{y_1 y_2} = \begin{bmatrix} c_{11} & c_{12} & \dots & c_{1m_2} \\ \vdots & \vdots & \ddots & \vdots \\ c_{m_1 1} & c_{m_2 2} & \dots & c_{m_1 m_2} \end{bmatrix}. \tag{4.9}$$

Based on equations 4.6 and 4.8, in order to construct the covariance matrix of the reduced dataset, we require the following ingredients:

1. covariance function of the original dataset,
2. number of PS per each spatial averaging cell,
3. the averaged covariance among the points per cell (i.e., $\bar{s}$)
4. the averaged cross-covariance among the points for each pair of cells (i.e., $\bar{c}$).

To even further reduce the number of the required ingredients, we tried to approximate the averaged covariances $\bar{s}$ and $\bar{c}$ as a function of the averaged distance among points. Let $C(h)$ be the spatial covariance model as a function of distance h. Then, the main question is whether it is possible to approximate the averaged covariances ($\bar{s}$ or $\bar{c}$) by the covariance of the averaged distances ($C(\bar{h})$). Or in other words, for an averaging cell with m number of points, can we write

$$\frac{1}{m}\sum_{i=1}^{m} C(h_i) = C\Big(\frac{1}{m}\sum_{i=1}^{m} h_i\Big) \quad ? \tag{4.10}$$

If so, we only need to store the average distance among points per cell (to compute $\bar{s}$ elements) and the average distance among points of pairs of cells (to compute $\bar{c}$ elements). The latter can be approximated as the distance between the centers of the averaging cells (assuming spatially homogeneous distribution of

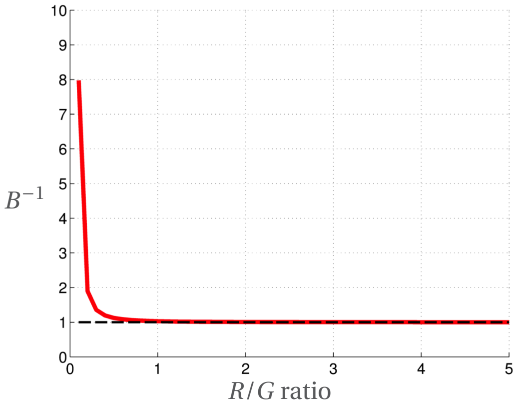

Figure 4.6: Level of over-estimation of the approximation of Eq. (4.10) for exponential covariance functions. The red curve shows the inverse of scaling factor B (of Eq. (4.13)) for different cell size (the horizontal axis shows the relative value of R/G). For $R/G > 0.5$ the B^{-1} value is close to one and the approximation is valid.

PS points within the cells). It is possible to show that for linear covariance functions (e.g. in the form of $C(h) = ah + b$), Eq. (4.10) is valid:

$$\frac{1}{m}\sum_{i=1}^{m} C(h_i) = \frac{1}{m}\sum_{i=1}^{m}(ah_i + b) = \frac{1}{m}\sum_{i=1}^{m} ah_i + \frac{1}{m}\sum_{i=1}^{m} b = a\bar{h} + b = C(\bar{h}). \tag{4.11}$$

In other words, for a linear covariance function, we can apply the error propagation (for the averaging) just based on the number of points and the average distance ($\bar{h}$). For nonlinear functions (e.g.,for Gaussian/exponential covariance functions), we can argue that the approximation of Eq. (4.10) is also valid but only for the range of distances in which the covariance function has a linear behavior. For the exponential model ($C(h) = \sigma^2 e^{-h/R}$), for example, we can write:

$$\frac{1}{m}\sum_{i=1}^{m} C(h_i) = \frac{1}{m}\sum_{i=1}^{m}\sigma^2 e^{-h_i/R} = \frac{1}{m}\sum_{i=1}^{m}\sigma^2 e^{-(\bar{h}+dh_i)/R} = \frac{\sigma^2}{m}\sum_{i=1}^{m}\left(e^{-\bar{h}/R}\times e^{-dh_i/R}\right) = C(\bar{h})\times\frac{1}{m}\sum_{i=1}^{m} e^{-dh_i/R} \tag{4.12}$$

Let the second term in the right hand side of above equation be equal to a scaling factor B (i.e., $B = 1/m\sum_{i=1}^{m} e^{-dh_i/R}$). Then, we can simplified the above equation as

$$\frac{1}{m}\sum_{i=1}^{m} C(h_i) = C(\bar{h})\times B. \tag{4.13}$$

For cases that the B value is close to one, we can effectively use the approximation of Eq. (4.10). In fact, when the dh_i values (deviation of distances from their mean) are much smaller than the correlation range (i.e., $dh_i \ll R$), the components $e^{-dh_i/R}$ get closer to one and so B is approximately equal to one. To demonstrate this fact, we run a simulation for an averaging cell containing 40 PS points, and we assumed an exponential covariance function. The location of PS points are homogeneously simulated in the cell. We also repeated the simulation for different cell size G (starting from 10 times bigger than the correlation range ($G = 10R$) to 5 times smaller than R or $G = 0.2R$). Fig. 4.6 shows the results of the simulation. The red curve in the figure shows the inverse of scaling factor B for different cell sizes (the horizontal axis shows the relative value of R/G). The results shows that the approximation is valid for averaging cells that are at least two times bigger than the correlation range (i.e., $R/G > 0.5$). For bigger cells, the proposed approximation underestimates the covariance values. As the covariance values for large distances are anyway less dominant (or insignificant), we argue that the approximation of Eq. (4.10) can be used effectively for the error propagation of the reduced datasets. Using this approximation together with equations 4.6 and 4.8, the variance of each spatial averaging cell and the covariances among the cells can be computed in a simple way as follows.

1. The variance of each cell is the function of number of points in the cell (m) and the average distance among the points $\bar{h}$:

$$\sigma_z^2 = \frac{\sigma^2}{m} + \frac{(m-1)}{m}C(\bar{h}). \tag{4.14}$$

Table 4.4: How to compute cov$\{Z_{G_i}^{T_p}, Z_{G_j}^{T_q}\}$: the covariance between the cell G_i at the averaging interval T_p and the cell G_j at the averaging interval T_q for the three contributing components of the covariance matrix. The temporal and spatial covariance functions are denoted as $C_t(.)$ and $C_s(.)$ respectively. It is assumed that there is no overlap between cells or between averaging intervals. Also these approximations are only valid for separable/distinct spatio-temporal covariance models such as the model of Eq. (4.4). The parameter m_i denotes the number of points in the cell G_i, the parameter n_p denotes the number of epochs/acquisitions in the averaging interval T_p, and $M = m_i n_p$. Also L_{ij} shows the distance between the centers of the cells G_i and G_j, ΔT_{pq} shows the time difference between intervals T_p and T_q, $\bar{h}_i$ is the averaged distance among the points of G_i, and $\Delta\bar{T}_p$ is the averaged time differences between dates of the acquisitions in the T_p interval.

	Nugget [Q_n]	Temporal component [Q_t]	Spatial component [Q_s]
$G_i = G_j,\ T_p = T_q$	$\frac{\sigma_0^2}{M}$	$\frac{\sigma_t^2}{M} + \frac{n_p-1}{M} C_t(\Delta\bar{T}_p)$	$\frac{\sigma_s^2}{M} + \frac{m_i-1}{M} C_s(\bar{h}_i)$
$G_i = G_j,\ T_p \neq T_q$	0	$\frac{C_t(\Delta T_{pq})}{m_i}$	0
$G_i \neq G_j,\ T_p = T_q$	0	0	$\frac{C_s(L_{ij})}{n_p}$
$G_i \neq G_j,\ T_p \neq T_q$	0	0	0

2. The covariance between the averaging cell z_1 containing m_1 points and the averaging cell z_2 containing m_2 points with the distance l_{12} between the two cells is computed as

$$\sigma_{z_1 z_2} = C(l_{12}). \tag{4.15}$$

Note that, by applying the proposed approximation, the derived covariances are not dependent on the number of points in the averaging cells in Eq. (4.15). In summary, by using the proposed approximation and having the covariance function $C(h)$ and the location of the averaging cells, we only require two ingredients to apply the error propagation: i) the number of points per averaging cell, ii) the average distance among points per cell ($\bar{h}$). These two values can be stored efficiently for each cell during the data reduction algorithm.

Data reduction in both the space and time domain

Using the same rationale of the previous section, it is possible to show that, for the spatio-temporal averaging, the covariance between the averaging cell G_i at the averaging interval T_p and the cell G_j at the averaging interval T_q for three contributing components of the covariance model of Eq. (4.4) can be computed using the equations in Table 4.4 (See the appendix for the proof). That is given the three covariance functions (i.e., the nugget effect, spatial component $C_s(.)$, and the temporal component $C_t(.)$), the full covariance matrix for the reduced dataset can be constructed using the following ingredients:

1. the coordinates of the center of the spatial averaging cells (to compute L_{ij} values in Table 4.4)
2. the time of the center of the averaging intervals (to compute ΔT_{pq} values in Table 4.4)
3. number of points per each spatial averaging cell (i.e., m_i in Table 4.4)
4. number of epochs/acquisitions in the averaging temporal intervals (i.e., n_p in Table 4.4)
5. averaged distances among the points of each spatial cell (i.e., $\bar{h}_i$ values in Table 4.4)
6. averaged time differences between dates of the acquisitions in each averaging temporal interval (i.e., $\bar{T}_p$ values in Table 4.4).

On positive semi-definiteness of the approximated covariance matrix

By definition, a covariance matrix must be positive semi-definite. The covariance functions that we used in this study are plausible covariance functions and so have the property that guarantees the positive semi-definiteness of the covariance matrices constructed with these functions. However, our proposed approximation does not necessarily provide a positive semi-definite covariance matrix. Different testing experiments

Table 4.5: Auto-correlation functions $\rho_{kl} = \mathrm{Corr}\{Z_{G_i}^{T_p}, Z_{G_j}^{T_q}\}$, corresponding to the covariance function of Eq. (4.4). The indices k and l are the indices of the cells $Z_{G_i}^{T_p}$ and $Z_{G_j}^{T_q}$, respectively.

	Nugget effect	Temporal component	Spatial component
$G_i = G_j,\ T_p \neq T_q$	0	$e^{-\frac{\lvert\Delta t_{pq}\rvert}{R_t}}$	0
$G_i \neq G_j,\ T_p = T_q$	0	0	$e^{-\frac{h_{ij}}{R_s}}$
$G_i \neq G_j,\ T_p \neq T_q$	0	0	0

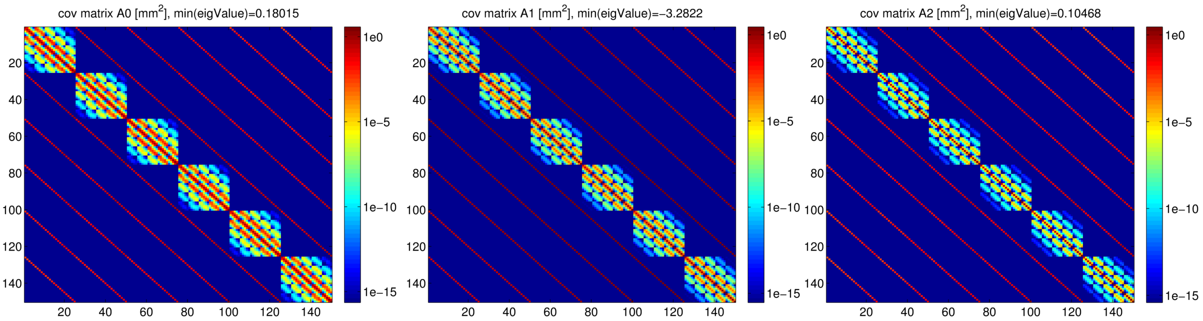

(a) Full Propagation (b) Proposed Approximation (c) Positive definite Approximation

Figure 4.7: Derived covariance matrices for the simulated scenario 1 (big grid-size).

indeed confirm that sometimes some Eigenvalues of the approximated matrix are negative. In order to constrain the approximation to be positive semi-definite, we propose a modification in the proposed approach as follows:

- the diagonal elements of the covariance matrix (i.e. the variances) are first derived based on the proposed approximation (using the first row of Table 4.4). Let's show the kth element of the covariance matrix by σ_k^2 corresponding to a spatio-temporal averaging cell $Z_{G_i}^{T_p}$.
- then, the off-diagonal elements σ_{kl} (i.e., covariances) are computed using the diagonal elements (σ_k^2 and σ_l^2) and the corresponding auto-correlation function (ρ_{kl}): $\sigma_{kl} = \sigma_k \sigma_l \rho_{kl}$.

The auto-correlation functions corresponding to the covariance function of Eq. (4.4) are summarized in Table 4.5. If k and l are the indices of the cells $Z_{G_i}^{T_p}$ and $Z_{G_j}^{T_q}$, respectively, the Table 4.5 shows the correlation between the two cells: $\rho_{kl} = \mathrm{Corr}\{Z_{G_i}^{T_p}, Z_{G_j}^{T_q}\}$. By using these plausible auto-correlation functions, the approximated matrix is always positive semi-definite.

4.4. APPLICATION ON A SIMULATED EXPERIMENT

To evaluate the performance of the proposed approximation method, we performed a test on two different simulated scenarios. We used the same covariance function that was estimated from the RadarSAT2 dataset (Table 4.2). The parameters of the two scenarios are summarized in Table 4.6. For each scenario, three different propagation approach have been applied: i) full error propagation, ii) the proposed approximation (Table 4.4), and iii) the proposed approximation with the positive semi-definiteness constraint (via the use of auto-correlation functions). Figs 4.7 and 4.8 show the calculated covariance matrices. Generally, the pattern and structure of the approximated covariance matrices are similar with the one derived from full propagation. However, the differences in the values are more significant for the 2nd scenario with small averaging intervals. Also note the negative eigenvalues of the matrices approximated without the positive semi-definiteness constraint, confirming that we should use the approximation always with the constraint. To get more insight,

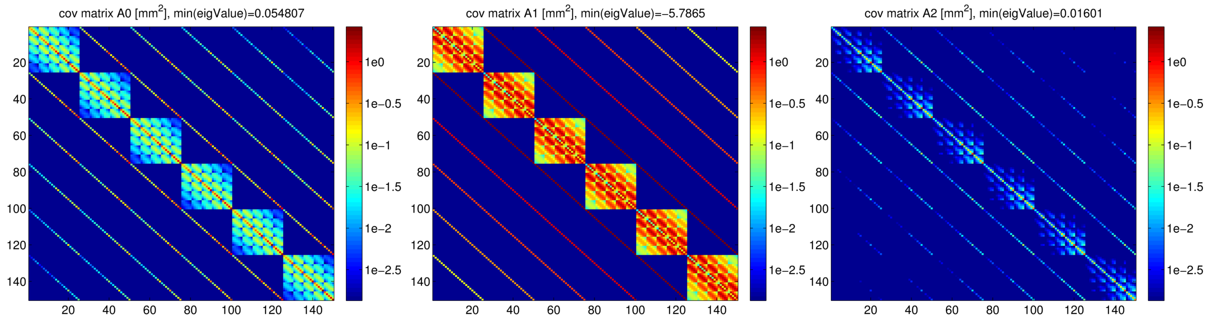

(a) Full Propagation (b) Proposed Approximation (c) Positive definite Approximation

Figure 4.8: Derived covariance matrices for the simulated scenario 2 (small grid-size).

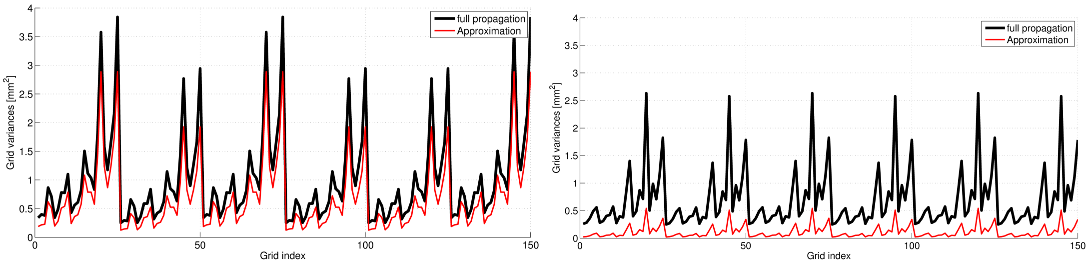

(a) Scenario 1: big grid-size (b) Scenario 2: small grid-size

Figure 4.9: Comparison between diagonal elements of the covariance matrices derived from full propagation versus from positive-definite approximation (a: big grid-size scenario, b: small grid-size scenario). Note that the number of epochs per averaging interval is larger in the second scenario (due to a different revisit time, see Table 4.6), resulting in smaller variances.

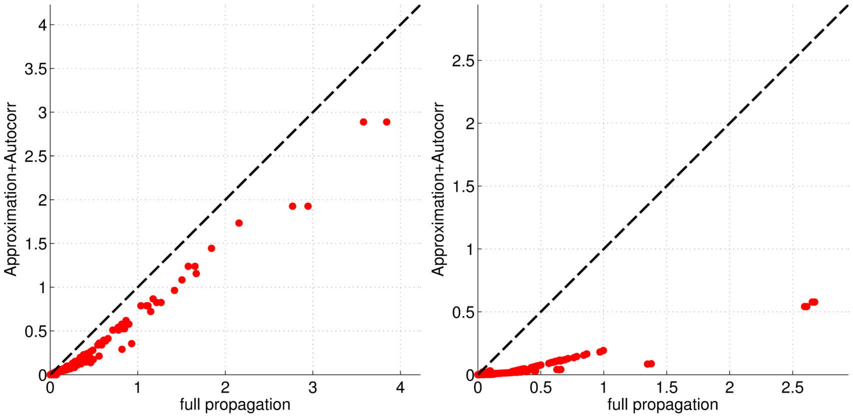

(a) Scenario 1: big grid-size (b) Scenario 2: small grid-size

Figure 4.10: Comparison between all the elements of the covariance matrices derived from full propagation versus from positive-definite approximation (a: big grid-size scenario, b: small grid-size scenario).

Table 4.6: Parameters of the two simulated scenarios.

Scenario	Number of PS	Area	Spatial grid	Period	Revisit period	Temporal intervals
Big grid	500	50×50 km^2	10 km	3 years	70 days	6 months
Small grid	500	5×5 km^2	1 km	3 years	11 days	6 months

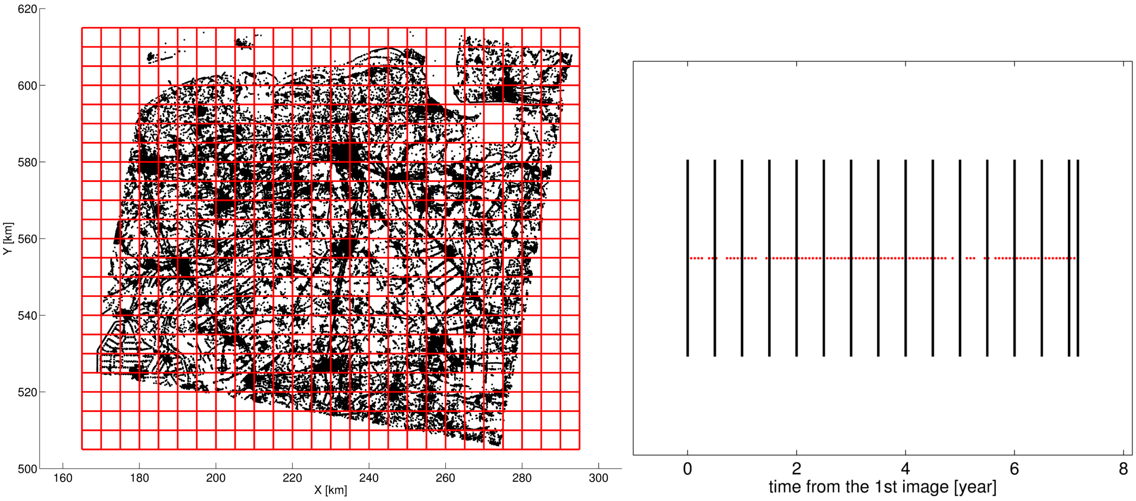

(a) Spatial Grid.

(b) Temporal Grid. Note that the number of epochs per averaging interval is different. This may result in different variances at different epochs.

Figure 4.11: Extent of the spatial and the temporal averaging intervals for data reduction applied on RadarSAT2 data.

Fig. 4.9 shows the comparison between the diagonal elements of the covariance matrices derived from the full propagation versus from the positive-definite approximation. Here we also see the underestimation of the variance values especially for the smaller grid-size scenario. Also in Fig. 4.8, we can see the comparison between all the elements of the covariance matrices derived from the two methods, and again the underestimation for the 2nd scenario is significant. However, we should note a linear dependency and the high correlation between the approximated values and the ones from the full propagation (the correlation coefficient is 0.99 and 0.93 for the two scenarios respectively). These high correlation coefficients confirm that the proposed approximation can construct the covariance matrices with the correct structure. However it usually underestimates the (co)variance values, especially for small grid intervals. The underestimation is mainly linear and up to a scaling factor. In real practice, it is recommended to perform a similar simulation study to estimate the scaling factor and to up-scale the approximated covariance matrices.

4.5. APPLICATION ON RADARSAT2 DATA

As a demonstration of the proposed method, we applied it on the RadarSAT2 dataset (see Section 4.2). A spatial grid size of 5 km[1] and a temporal grid of 6 months have been chosen. Fig. 4.11 shows the extent of the spatial and the temporal averaging intervals. The results of the data reduction are visualized in Fig. 4.12. The approximated covariance matrix for the reduced dataset has been derived from the proposed approach of the previous section and visualized in Fig. 4.13. To see more details of the structure of the contributing covariance matrices (i.e., nugget effect, temporally correlated component, and spatially correlated component), we plot the sparsity pattern of these contributions in Fig. 4.14. By using the proposed approximation, the error propagation has been computed in few seconds.

---

[1] Note that the choice of a 5 km grid size is not suggested based on the analysis of Fig. 4.6. To have a valid approximation, it was suggested to have spatial grid cells smaller than $2R$ (e.g., for RadarSAT2 data, R =1.1 km) and so the grid size should be smaller than 2.2 km. However, for the sake of demonstration in this chapter and to avoid large covariance matrices, we choose a 5 km grid. Note that the induced underestimation does not affect the sparsity pattern of the derived covariance matrices in Fig. 4.14.

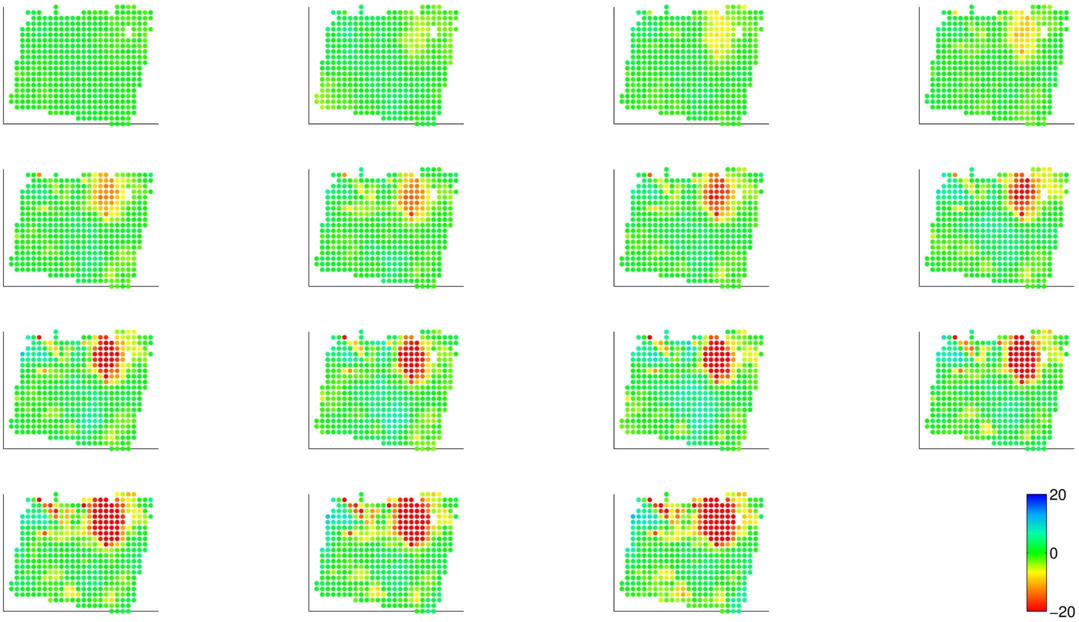

Figure 4.12: Results of data reduction on PS deformation of the Groningen area derived from the RadarSAT2 dataset acquired between September 2009 and November 2016 (In total: 15 averaging intervals in the time domain). Color scale is in mm^2.

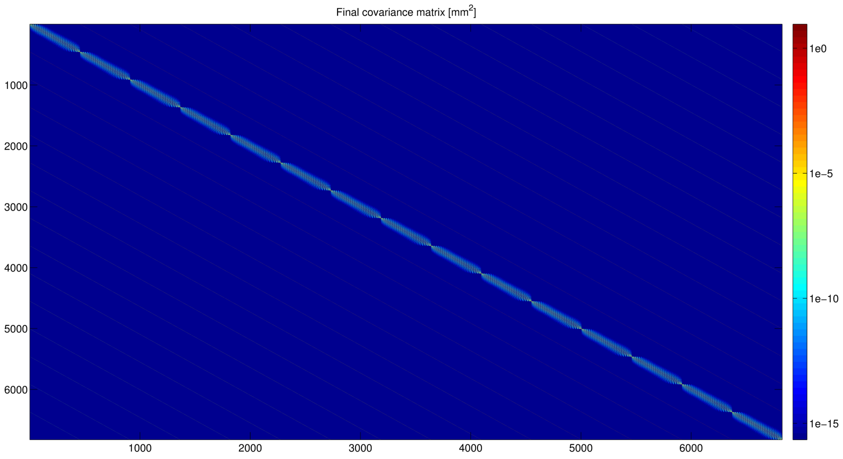

Figure 4.13: The approximated covariance matrix for the reduced RadarSAT2 dataset. Note the logarithmic color-scale in [mm^2].

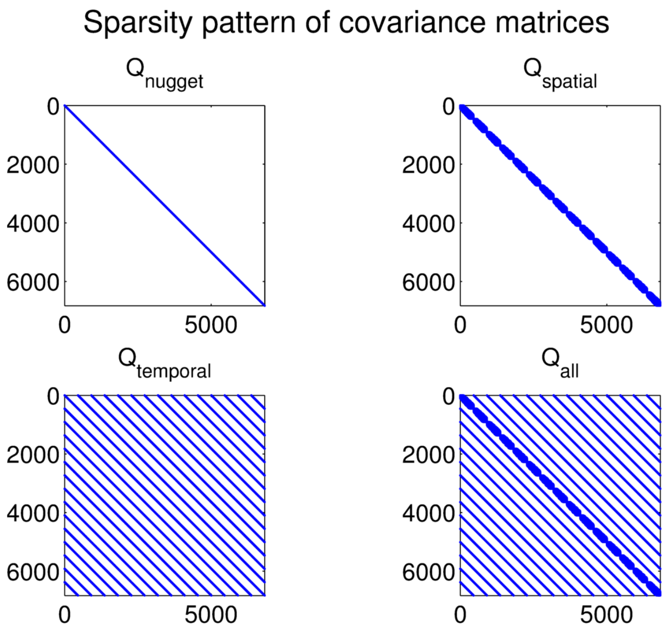

Figure 4.14: Sparsity pattern of the contributing factors in the approximated covariance matrix for the reduced RadarSAT2 dataset.

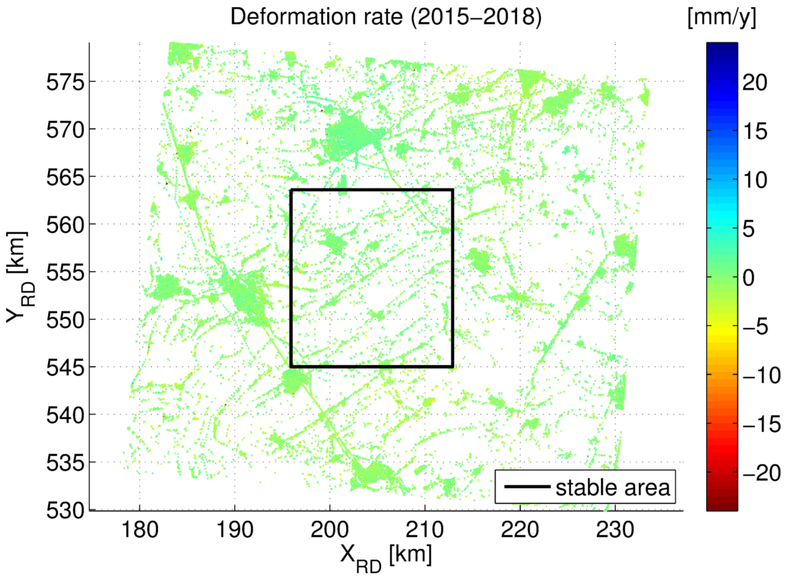

Figure 4.15: PSI velocity map of the Groningen area based on the Sentinel-1 dataset acquired between November 2015 and October 2018. The black box shows the selected signal-free area.

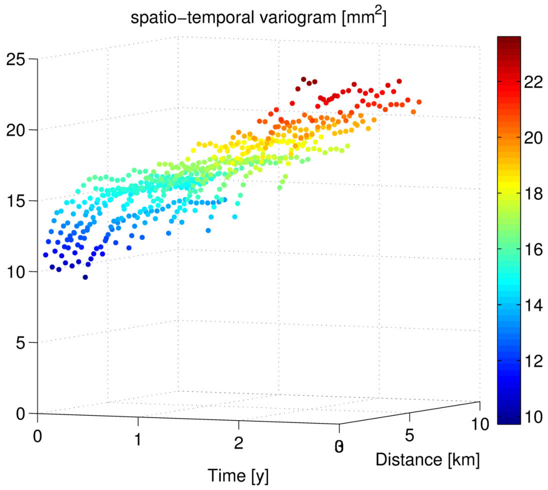

Figure 4.16: Empirical spatio-temporal variograms of Sentinel-1 InSAR data over the signal-free area.

Table 4.7: Estimated parameters for spatio-temporal variogram model for model of Eq. (4.4) for Sentinel-1 dataset. (selected as the proper model for this study).

σ_0^2 [mm^2]	σ_t^2 [mm^2]	R_t [years]	σ_s^2 [mm^2]	R_s [km]
9.49	4.53	0.70	4.96	1.09

4.6. STOCHASTIC MODELING: SENTINEL-1 DATA

So far all the results have been obtained based on the noise parameters derived from an assumed stable area in RadarSAT2 dataset (see Table 4.2). In order to apply the proposed method on Sentinel-1 data, we should estimate the noise parameters from a Sentinel-1 dataset. In order to evaluate the spatio-temporal variability of measurement noise, we analysed a Sentinel-1 dataset over the presumably signal-free area close to Groningen region. The dataset containing 133 radar images acquired between November 2015 and October 2018 was used for the study.

Fig. 4.15 shows the selected study area (box of ~17×17 km) for the analysis. The same procedure as for the RadarSAT2 data has been applied here (see Section 4.2). The obtained empirical variograms are visualized in Fig. 4.16. The covariance function of the model in Eq. (4.4) has been fitted to the empirical variograms. The results are presented in Figs. 4.17 and 4.18, and Table 4.7 reports the estimated parameters of the variogram model. The estimated parameters are almost similar to the model parameters of RadarSAT2 (compare Tables 4.2 and 4.7), except the nugget effect that is a bit larger for the Sentinel-1 dataset.

4.7. SPATIO-TEMPORAL ANALYSIS: SENTINEL-1 DATA

As presented in Chapter 2, in order to study the effect of different atmospheric mitigation methods, four scenarios have been investigated: i) conventional approach, ii) no atmosphere mitigation, iii) ECMWF correction plus conventional approach, and iv) ECMWF correction only. To get more insight to the spatio-temporal variability of noise components in these four approaches, we estimated empirical variograms over the presumably stable area (see Section 4.2) for all these scenarios. Fig. 4.19 shows the spatio-temporal variograms. The results show that the application of ECMWF correction does not have significant added value in reducing the atmospheric noise variability. Also the comparison between the conventional approach and the ECMWF+conventional approach shows that applying ECMWF slightly increases the noise variability. We can conclude that, the ECMWF models (with their current progress status) cannot mitigate atmospheric noise in a reliable and accurate manner, especially in the flat areas like Netherlands in which the main atmospheric artifacts are induced by turbulent mixing. This confirms the study of Liu (2012) that has concluded that: *"con-*

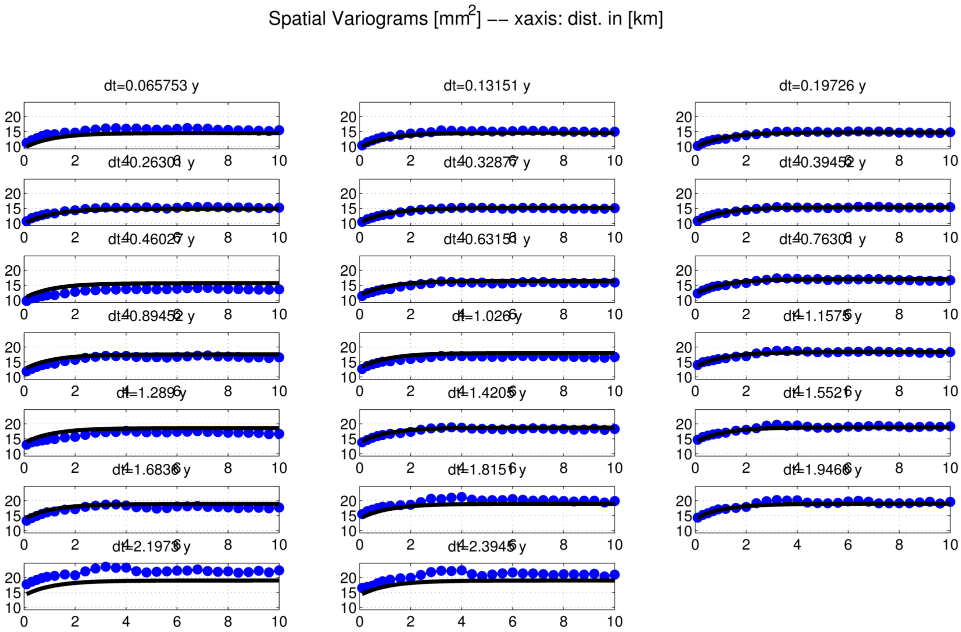

Figure 4.17: Fitted model to the Spatial variogram profiles of Sentinel-1 InSAR data over the signal-free area for different temporal lags (from 0.06 to 3.8 years). The horizontal axes are labeled by spatial lag in [m], and vertical axes display the variograms in [mm^2].

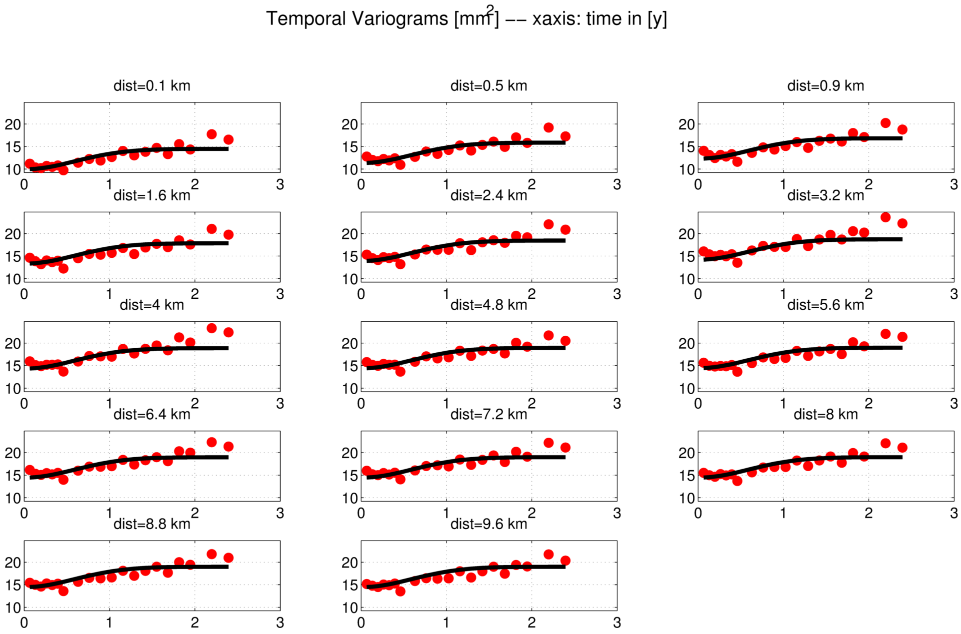

Figure 4.18: Fitted model to the temporal variogram profiles of of Sentinel-1 InSAR data over the signal-free area for different spatial lags (from 100 meter to 10 km). The horizontal axes are labeled by temporal lag in [years], and vertical axes display the variograms in [mm^2].

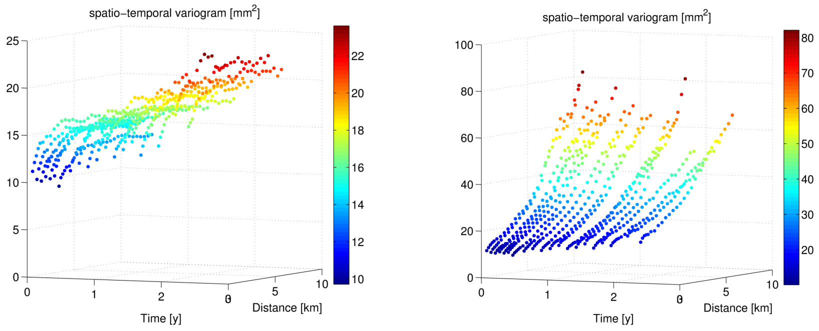

(a) Conventional approach

(b) No atmosphere mitigation

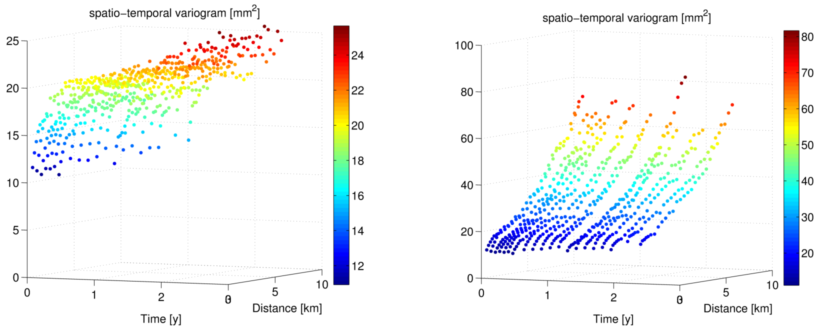

(c) ECMWF correction+conventional approach

(d) ECMWF correction only

Figure 4.19: Spatio-temporal variograms for different atmospheric mitigation methods.

temporary weather models are useful for correcting the height dependent delay in interferograms over mountainous regions, however ... for correcting delay caused by turbulent mixing, the value of these models is very limited and we recommend not to use them for APS correction."

4.8. SUMMARY

In this section, we provide an analytical formulation and a step-wise algorithm to calculate the variances of all spatio-temporal deformation measurements and covariances among them. The measurement noise properties of InSAR data over the Groningen area for both RadarSAT2 and Sentinel-1 datasets were investigated through a spatio-temporal variogram analysis over a stable (signal-free) area. The results showed the presence of three different noise components in the data: i) white noise (nugget effect), ii) spatially correlated noise, and iii) temporally correlated noise. The modeling of the empirical variograms showed that the temporal and the spatial components can be modeled in a dis-joint manner. For the both RadarSAT2 and Sentinel-1 datasets, the parameters of the noise components were estimated.

Furthermore, we proposed a simple analytical approximation to propagate the covariance matrix of InSAR data to the covariance matrix of reduced datasets. Note that we only considered averaging-based reduction methods, i.e., methods that are based on unweighted averaging, either in time, in space, or in both. The proposed approach has been tested and validated via a simulated study and was demonstrated on RadarSAT2 data. The proposed approximation can construct the covariance matrices with a correct structure. However, it usually underestimates the (co)variance values, especially for small averaging intervals. The underestimation is mainly linear and can be mitigated by calibrating a scaling factor.

5

FUNCTIONAL MODEL IDENTIFICATION

5.1. INTRODUCTION

Persistent Scatterer Interferometry provides surface deformation measurements with millimetric precision. The technique is based on time series analysis of consistent satellite radar reflections of the surface. The information content of a particular deformation measurement is dependent on the origin of the reflective object, including the its subsurface foundation, see Fig. 5.1. Specular reflections from an object and dihedral wall–terrain reflections have a different sensitivity to the mechanisms driving the deformation. Roughly, three categories of these causes can be identified:

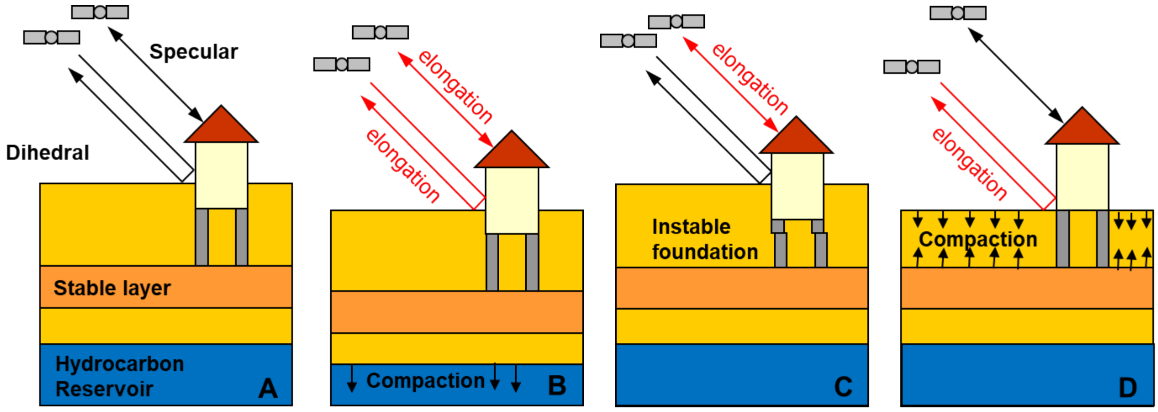

Figure 5.1: Sensitivity of PSI measurements for different deformation regimes. A) Dihedral wall-terrain reflections are sensitive to motion of the terrain layer and deeper layers, whereas, in case of deep foundations, specular reflections from objects are only sensitive to motion of the foundation layer due to deep processes. B) The effect of deep compaction, measured by both the dihedral and specular reflections. C) The effect of an instable foundation, only measured by the specular reflections. D) The effect of shallow compaction, only measured by the dihedral reflections.

1. ‘Deep’ causes, e.g., due to oil, gas or salt extraction, ground water pumping, or other types of mining,
2. ‘Shallow’ causes, e.g., peat oxidation, compaction of deposits,
3. Object-related causes, e.g., degradation or thermal expansion of buildings and infrastructure.

As Fig. 5.1 shows, each radar reflection is sensitive to two or more deformation causes. This is summarized in Table 5.1. The table shows that all reflections are sensitive to the deformation caused by deep processes. However, for the shallow processes and object-related effects, this differs. The classification made in Table 5.1 is a general indication of sensitivity. Deviations will occur. For instance, a tilt of a building due to foundation instability will also affect the wall-terrain reflection obtained. For many applications, an estimate of the surface deformation due to one specific cause, e.g., due to gas extraction, is desired. Ideally, the deformation time series of each detected consistent radar reflection, a so-called Persistent Scatterer, is decomposed in the

Table 5.1: Sensitivity of radar reflections to deformation due to different causes.

Reflection origin	Deep	Shallow	Object
Object with deep foundation (pile-supported)	X		X
Object with shallow foundation	X	X	X
Terrain	X	X	

different deformation regimes. However, this is not feasible based on a single PS and associated deformation time series. Instead, information of multiple scatterers should be used, possible in combination with auxiliary data.

Various methodologies have been proposed to separate different deformation regimes:

1. Statistical analysis of PS per spatial grid cell (see Bruna (2020), http://www.bodemdalingskaart.nl).
2. Classification of PS.
    (a) Based on separation of even and odd bounces of the radar signal using different radar polarization bands (Ketelaar, 2009, Perissin, 2006).
    (b) Based on auxiliary data, e.g., detailed databases with outlines of buildings and other infrastructure (Bruna, 2020).
    (c) Based on high-low scatterer height separation (Dheenathayalan, 2019).
    (d) Based on deformation time series.
        i. Machine learning (van de Kerkhof et al., 2018, van De Kerkhof et al., 2020).
        ii. Decomposition, e.g., splines (van der Marel, 2020).
        iii. Multiple Hypothesis Testing (MHT) (Chang and Hanssen, 2015).

Here, we present and evaluate the Multiple Hypothesis Testing approach. The advantage of this approach is that it enables the incorporation of the stochastic model of the observations. Hence, the stochastic model derived in Chapter 4 is used in the analysis.

5.2. BACKGROUND

The objective of testing in geodesy is to detect and adapt inconsistencies between 1) the functional model, 2) the stochastic model, and 3) the observations, using a certain set of testing parameters (Baarda, 1968, Teunissen, 2000). For conventional geodetic measurement techniques, the majority of these factors is sufficiently well known, e.g., by using a single instrument to measure a redundant network between well-defined benchmarks. This enables for instance the detection of measurement errors or the estimation of stochastic model parameters.

The problem in InSAR time series parameter estimation and testing is that both the functional model as well as the stochastic model are in principle unknown and different for each scatterer. As discussed in the introduction, the scatterer is sensitive to the sum of sub-surface and object-related processes, which ideally should be described by the functional model as much as possible. Regarding the stochastic model, the scattering noise ('clutter') introduces a specific stochasticity per individual scatterer, which can vary from epoch to epoch. Moreover, scatterers may change temporarily (e.g., due to snow cover), or become obscured by another object blocking the radar reflection (e.g., a parked car). The uncertainty in both the functional and the stochastic model makes the use of Multiple Hypothesis Testing (MHT) for model selection and/or the clustering of Persistent Scatterers into different deformation regimes a non-trivial task.

There are different, possibly inter-related, objectives of applying Multiple Hypothesis Testing (MHT) to Persistent Scatterer time series, .e.g.,

1. to obtain the best (optimal, efficient, realistic) functional representation of the true deformation behavior of the point, and thereby to improve the interpretation,
2. to classify scatterers (e.g., showing a temperature related effect or not) to improve further interpretation,
3. to prevent ‘leakage’ of actual deformation signal in other deterministic parameters, e.g., height estimates or atmospheric signal delays,
4. to prevent ‘leakage’ of actual deformation signal components into the stochastic model, or
5. to detect changes (sudden motion or rate changes) for anomaly detection.

These objectives have in common that an optimal functional representation is searched for. However, the functional models used should not simply be extended with additional parameters, without a stochastic justification of this extension. Hence, the additional model parameters should be statistically significant. To test this, Multiple Hypothesis Testing can be applied.

5.3. METHODOLOGY

The basic concept of Multiple Hypothesis Testing is to confront the null hypothesis H_0 with a number of alternative hypothesis H_j. These hypothesis are denoted as

$$\begin{aligned} H_0: \quad E\{\underline{y}\} &= Ax \quad ; \quad D\{\underline{y}\} = Q_{yy}, && (5.1)\\ H_j: \quad E\{\underline{y}\} &= Ax + C_j \nabla_j \quad ; \quad D\{\underline{y}\} = Q_{yy}, && (5.2) \end{aligned}$$

where $E\{.\}$ is the expectation operator, $\underline{y}$ is the vector of m observations, A is the design matrix, and x the vector of n unknown parameters. The dispersion D of the observations is described by the covariance matrix Q_{yy}. The alternative hypotheses are provided by an extension of the null hypothesis, described by the matrix C_j, to estimate the additional parameters ∇_j. The dimension or *degree of freedom* of ∇_j is indicated by q, with $q \in [1, m-n]$. Acceptance or rejection of H_0 is based on the test statistic $\underline{T}_j^q$ (Teunissen, 2000)

$$\underline{T}_j^q = \underline{\hat{e}}_0^T Q_{yy}^{-1} \underline{\hat{e}}_0 - \underline{\hat{e}}_j^T Q_{yy}^{-1} \underline{\hat{e}}_j. \tag{5.3}$$

Here, $\underline{\hat{e}}_0$ and $\underline{\hat{e}}_j$ are the residuals under the null and a particular alternative hypothesis, respectively, $(.)^T$ indicates the transpose and $(.)^{-1}$ the inverse. Note that the value of the test statistic is always non-negative, as the residuals under the null hypothesis are always larger or equal to the residuals under the alternative hypothesis. The test statistic has a χ^2-distribution with q degrees of freedom

$$\begin{aligned} H_0 \quad &: \quad \underline{T}_0^{q=m-n} \sim \chi^2(q, 0), \\ H_j \quad &: \quad \underline{T}_j^q \sim \chi^2(q, \lambda), \end{aligned} \tag{5.4}$$

where λ is the non-centrality parameter

$$\lambda = \nabla_j^T C_j^T Q_{yy}^{-1} Q_{\hat{e}_0\hat{e}_0} Q_{yy}^{-1} C_j \nabla_j, \tag{5.5}$$

with

$$Q_{\hat{e}_0\hat{e}_0} = Q_{yy} - A(A^T Q_{yy}^{-1} A)^{-1} A^T \tag{5.6}$$

A critical value k_α is used to determine whether the H_0 should be rejected

$$\text{reject } H_0 \text{ if } \underline{T}_j^q > k_\alpha. \tag{5.7}$$

The critical value is determined from the χ^2-distribution with q degrees of freedom by choosing a *level of significance* α, see Fig. 5.2. The relation between α and k_α is denoted by

$$\alpha(q) = \int_{k_\alpha}^{\infty} P(\chi^2 | q, 0)\, d\chi^2, \tag{5.8}$$

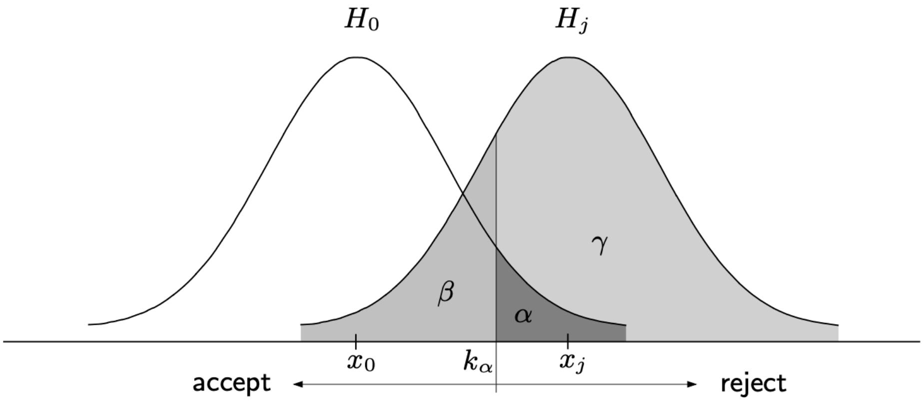

Figure 5.2: The concept of hypotheses testing. The null hypothesis H_0 is compared to an alternative hypothesis H_j. The test statistic $\underline{T}_j^q$ in relation to the critical value k_α determines whether the null hypothesis is accepted or rejected. The critical value is based on the chosen level of significance α. The α represents the probability of incorrect rejection of H_0, known as a Type-I error. The opposite error, incorrect acceptance of H_0, is denoted as a Type-II error. The probability of this error is indicated by β. Often, the power of the test $\gamma = 1-\beta$ is used, i.e., the probability that H_0 is correctly rejected.

where $P(.)$ is the probability density distribution. The α represents the probability of incorrect rejection of H_0 and should be as low as possible. Typical values for α are within the range 0.001-0.05. Such an incorrect rejection of H_0 is known as a *Type-I error*. The opposite error, incorrect acceptance of H_0 is denoted as a *Type-II error*. The probability of a Type-II error is equal to β, as indicated in Fig. 5.2. In geodesy, instead of β often the *power of the test* $\gamma = 1-\beta$ is used, i.e., the probability that H_0 is correctly rejected. The power of the test is a function of α, q and λ

$$\gamma(\alpha, q, \lambda) = \int_{k_\alpha}^{\infty} P(\chi^2|q,\lambda)d\chi^2. \tag{5.9}$$

A typical applied value of γ is 0.8 (Teunissen, 2000). However, when tests of different dimensions are compared, a value of 0.5 should be applied, as will be discussed later.

To reduce the probability of the two types of errors, both α and β should be as small as possible, ideally zero. However, if α is chosen smaller, β increases, and vice versa, see Fig. 5.2. To define a test that copes with this paradox, the Neyman-Pearson principle is applied (Neyman and Pearson, 1933). This principle states that from all tests with the same probability of Type-I errors, the one for which the chance of Type-II errors is as small as possible should be used. The test statistic $\underline{T}_j^q$ is a consequence of this principle (Teunissen, 2000).

The special case of $q = m-n$ indicates the most relaxed alternative hypothesis possible, which leaves the observables completely free (Teunissen, 2006). As a result, the residuals $\hat{\underline{e}}_j$ under this alternative hypothesis are equal to zero, and the test statistic (Eq. (5.3)) reduces to

$$\underline{T}_0^q = \hat{\underline{e}}_0^T Q_{yy}^{-1} \hat{\underline{e}}_0. \tag{5.10}$$

This test checks the overall validity of H_0 and is there denoted as the *Overall Model Test* (OMT). The advantage of this test is that the validity of H_0 can be tested without the need to specify any particular alternative hypothesis (Teunissen, 2006). When H_0 is rejected, this indicates that either the functional model used is not describing the observations sufficiently well, or that the assumed stochastic model applied is too optimistic. To find a better fitting functional model, alternative hypothesis can be tested, again using the test statistic. This can be done rather efficient for a large dataset of PS time series, and a range of different alternative models. To show this, the expression for the test statistic Eq. (5.3) can be re-written as (see Teunissen (2000) for the derivation)

$$\begin{aligned} \underline{T}_j^q &= \hat{\underline{e}}_0^T Q_{yy}^{-1} \hat{\underline{e}}_0 - \hat{\underline{e}}_j^T Q_{yy}^{-1} \hat{\underline{e}}_j, \\ &= \hat{\underline{e}}_0^T Q_{yy}^{-1} C_j (C_j^T Q_{yy}^{-1} Q_{\hat{e}_0\hat{e}_0} Q_{yy}^{-1} C_j)^{-1} C_j^T Q_{yy}^{-1} \hat{\underline{e}}_0, \\ &= \hat{\underline{e}}_0^T L_j \hat{\underline{e}}_0. \end{aligned} \tag{5.11}$$

Hence, assuming that Q_{yy} is equal for all PS time series, the matrix L_j only needs to be computed once for each alternative hypothesis, and all test statistics can be computed efficiently for potentially millions of PS in the dataset based on the residuals under H_0.

The remaining problem is to determine which alternative model is the best. In case the alternative hypotheses have different dimensions, their test statistics have a different χ^2-distribution, and thereby a different critical value k_{α_q} for a set of pre-defined testing parameters. To overcome this problem, the concept of test quotients (de Heus et al., 1994) is used. The test quotient $\underline{\boldsymbol{T}}_j^q$ is defined as the ratio between the test statistic and the corresponding critical value, hence

$$\underline{\boldsymbol{T}}_j^q = \frac{\underline{T}_j^q}{k_{\alpha_q}}. \tag{5.12}$$

Each H_j with a test quotient larger than one is more favorable compared to H_0. The H_j with the largest test statistic is rejecting the H_0 most significantly, and is therefore adopted. Only in case all H_j are smaller or equal to one, there is no reason to reject H_0 after all. Note that the test quotient is a heuristic measure to overcome the problem of comparing tests with different degrees of freedom. When the degree of freedom is different, the selection of the most correct model is not guaranteed (Teunissen, 2017, Teunissen et al., 2020, Tiberius, 1998, Zaminpardaz and Teunissen, 2018).

Although the test quotients enable the comparison of alternative hypothesis, this comparison is still influenced by the selection of the test parameters α_q and γ_q. In principle, an equivalent error at different dimensions should be detected with equal probability. This probability is referred to as the power of the test γ. To minimize the chance of inconsistencies between tests of different dimensions, the *B-method* of testing is developed (Baarda, 1968, Teunissen, 2000). The essence of the B-method of testing is to adopt a reference power of the test γ_0, and to select a level of significance α_1 for the one-dimensional test. It is shown by de Heus et al. (1994), Kampes (2006) that it is essential to set γ_0 to 0.5 to ensure that the most significant alternative hypothesis among tests of different dimensions is identified. Once these values are set, the corresponding non-centrality parameter λ_0, and subsequently the α_q values for any dimension can be calculated using the relation

$$\lambda_0 = \lambda(\alpha_q, q, \gamma_0). \tag{5.13}$$

Based on the α_q values obtained for the different degrees of freedom in the library of alternative hypothesis, the corresponding critical values k_{α_q} can be calculated. Based on these critical values, the Test quotients (Eq. (5.12)) can be computed, and the most significant alternative hypothesis can be identified.

5.3.1. TESTING STRATEGIES

There are different strategies to apply a multiple hypothesis testing theory, as presented in the previous section, to Persistent Scatterer deformation time series. Here, we evaluate three alternative approaches:

1. **Model extension test approach**.
2. **Sequential Overall Model Test approach**.
3. **Minimal Overall Model Test approach**.

Each of these methods are described in the next sections.

MODEL EXTENSION TEST

The model extension test approach is based on the comparison of a null hypothesis H_0 with a library of alternative hypothesis $H_j, \forall j$. This approach follows the Detection, Identification and Adaptation (DIA) procedure (Chang and Hanssen, 2015, Teunissen, 1990). First, the Overall Model Test (OMT, Eq. 5.10) is used to assess whether the null hypothesis describes the PS time series sufficiently well. If the H_0 is rejected, the test quotients of a pre-defined library of alternative hypothesis are computed. The H_j with the largest test quotient, which indicates the largest improvement with respect to H_0, is *identified* as the most likely H_j. This can be seen by observing the general expression for the test statistic (Eq. (5.3)). The test statistic can also be interpreted as the difference between the OMT of H_0 and H_j. Hence, the larger the test statistic, the larger the difference, and thereby improvement, of the particular H_j. By using the test quotient, the difference in the degree of freedom of the various H_j is accounted for.

In case the maximum value of the test quotients of the H_j is lower than one, this indicates that the improvement by the alternative hypotheses is not significant with respect to H_0, and therefore there is no reason to reject H_0 after all.

The procedure followed results in a strong difference in the role of H_0 with the respect to the potentially numerous H_j. That is, H_0 is accepted when it describes the deformation time series sufficiently well, whereas in case of rejection, the *best* fitting alternative is adopted as the most appropriate model. This library of alternative models could also contain extensions of each other. Furthermore, the model extension test approach can only be applied if the alternative hypothesis are an extension of H_0. To circumvent this restriction, and the imbalance between the position of H_0 compared to the alternative hypothesis, the sequential Overall Model Test approach can be used.

SEQUENTIAL OVERALL MODEL TEST

In the sequential Overall Model Test (OMT) approach the OMT $T^q_{0_j}$ of a library of models is assessed in sequential order. The approach is based on the procedure proposed by Lindenbergh and Hanssen (2003), however is refined by including the B-method of testing, to increase the equality between tests with different degrees of freedom. The essence of the approach is that in the first iteration, all models with the highest degree of freedom, hence, with the lowest amount of parameters, are evaluated. This can be one or multiple models. In case the lowest Test quotient $\underline{\boldsymbol{T}}^q_{0_j}$ for a particular PS time series is smaller than one, this model is accepted, hence

$$\text{accept } H_{0_j} \text{ if } \underline{\boldsymbol{T}}^q_{0_j} \leq 1 \quad \text{and} \quad \min_j\{\underline{\boldsymbol{T}}^q_{0_j}\},\ \forall j. \tag{5.14}$$

Only for those PS time series where no model is accepted, a new set of models, with a lower degree of freedom, is evaluated. This procedure is repeated sequentially, until all models in the library have been evaluated. In case none of the models results in a Test quotient lower than one, the particular PS remains unclassified. Alternatively, the lowest test quotient in the last iteration, even if the values is larger than one, could be adopted.

The consequence of the Sequential Overall Model Test approach is that a certain model is adopted for a PS once the fit to the time series is *acceptable*. This does not mean that the *best* model in the library is selected. In case the objective of the testing approach is the selection of the best model, an alternative approach is needed, the Minimal Overall Model Test approach.

MINIMAL OVERALL MODEL TEST

In the Minimal Overall Model Test (OMT) approach all models in the library are treated equally. Hence, for each model the Test quotient of the OMT $\underline{\boldsymbol{T}}^q_{0_j}$ is calculated, and the model with the lowest test quotient is adopted. That is

$$\text{accept } H_{0_j} \text{ if } \min_j\{\underline{\boldsymbol{T}}^q_{0_j}\},\ \forall j. \tag{5.15}$$

By applying the B-method of testing, hence, by adapting the critical value k_α used based on a fixed power of the test γ_0, the difference in the degree of freedom of the different models is accounted for. This procedure may suggest large similarity with the Model extension approach, although in this approach there is no special role of a null hypothesis and the model with the smallest Test quotient (best fitting model to the data), instead of the largest test quotient of the alternative hypothesis (largest improvement with respect to the null hypothesis).

5.4. RESULTS

The three different approaches described in Section 5.3 are implemented and tested. First, the approaches are evaluated based on simulated data, see Section 5.4.1. Based on the results, the most suitable approach is selected. This approach is applied to a real dataset of the Groningen gas extraction region in the Netherlands, see Section 5.4.2.

5.4.1. SIMULATION

To assess the performance of the testing approaches described, a dataset of 100000 PS is simulated, based on the acquisition dates of 68 RadarSAT-2 images, covering a time span of almost 5 years. For each PS, a deformation time series is simulated using a sample of a uniform distribution of linear deformation rates between +/- 30 mm/y, a seasonal signal with an amplitude between 0 and 20 mm, and uncorrelated normally distributed measurement noise with a standard deviation of 5 mm.

Based on these simulated data, the three hypothesis testing approaches are applied. Hereby, the B-method of testing is used, based on a γ_0 of 0.5 and an α_1 of $1/2m$, where m =68 images in this case. The α_1 of $1/2m$ is a heuristic rule proposed in de Heus et al. (1994), and also adopted in Chang and Hanssen (2015). As a first experiment, a zero-velocity model is assumed as H_0. Hence, only a constant offset[1] for each time series is estimated. This model is indicated as the constant model. As alternative hypothesis, the constant model extended with a linear deformation rate, and extended with a linear rate + periodic function with a period of 1 year are assessed. The result of the classification of the 100000 PS, using the true simulated values for the location in the plot, are shown in Fig. 5.3. The figure shows a remarkable effect in the results for the Model extension method. In case of large deformation rates, in combination with a large periodic amplitude, the constant+linear model is adopted as the best H_j (in green). Based on the simulated amplitudes applied for these points, a classification with the constant+linear+periodic model is expected (in blue). However, because the degree of freedom is larger for the H_j including the periodic signal, the critical value of this test is larger, resulting in a relative downscaling of the Test quotient of the periodic model compared to the linear model. This effect becomes relatively larger with increasing linear deformation rates, and is only partly compensated with an increasing amplitude of the periodic signal. This results in the triangular shape in the classification shown in the figure.

The Sequential OMT method results are more according to the the expectations. The clusters of the different adopted models are clearly visible. In case the simulated amplitude of the periodic signal exceeds a certain value, the adopted model changes from the constant+linear to the constant+linear+periodic model. There is no strict division line visible, because of the normal distributed measurement noise applied. The figure also shows that in many cases no model is assigned, since none of the test quotients had a value below one. This is different for the Minimal OMT method. Here, simply the lowest test statistic is selected, resulting by definition in a selected model for each PS. The figure indicates as well that less PS are assigned to the constant+linear cluster compared to the results obtained with the sequential approach. The is due to the difference in accepting the best model versus an acceptable model in a sequential manner.

As alternative to the constant model as H_0, a similar test is performed taking the constant+linear model as null hypothesis. The results for the simulated data are shown in Fig. 5.4. The figure shows that the artifact using the Model extension approach does not occur using this H_0 and that the results are as expected. For the OMT-based methods, the figures are very similar compared to the H_0 with the constant model only case, only the constant class is missing. By comparing the three outcomes, the main difference is in the level of transition between the constant+linear and the constant+linear+periodic model, with increasing amplitude of the periodic signal. This is due to the difference between selecting an acceptable model versus the best

---

[1] Note that a constant offset should always be estimated for PS time series, since the time series is relative in time. Typically, the first epoch is set to zero. However, this is an arbitrary choice. To avoid an erroneous large influence of the noise in the first epoch, a constant offset should be included in the model. The use of a constant model only without other parameters should be considered with care. Since PS time series are also relative in space, a possible 'constant' behavior of the complete time series is dependent on the reference applied. Only when this reference is determined sufficiently well, e.g., using collocated GNSS measurements at active or passive radar reflectors, PS classified as constant can be interpreted correctly. Moreover, the uncertainty in the reference should be considered in the stochastic model applied.

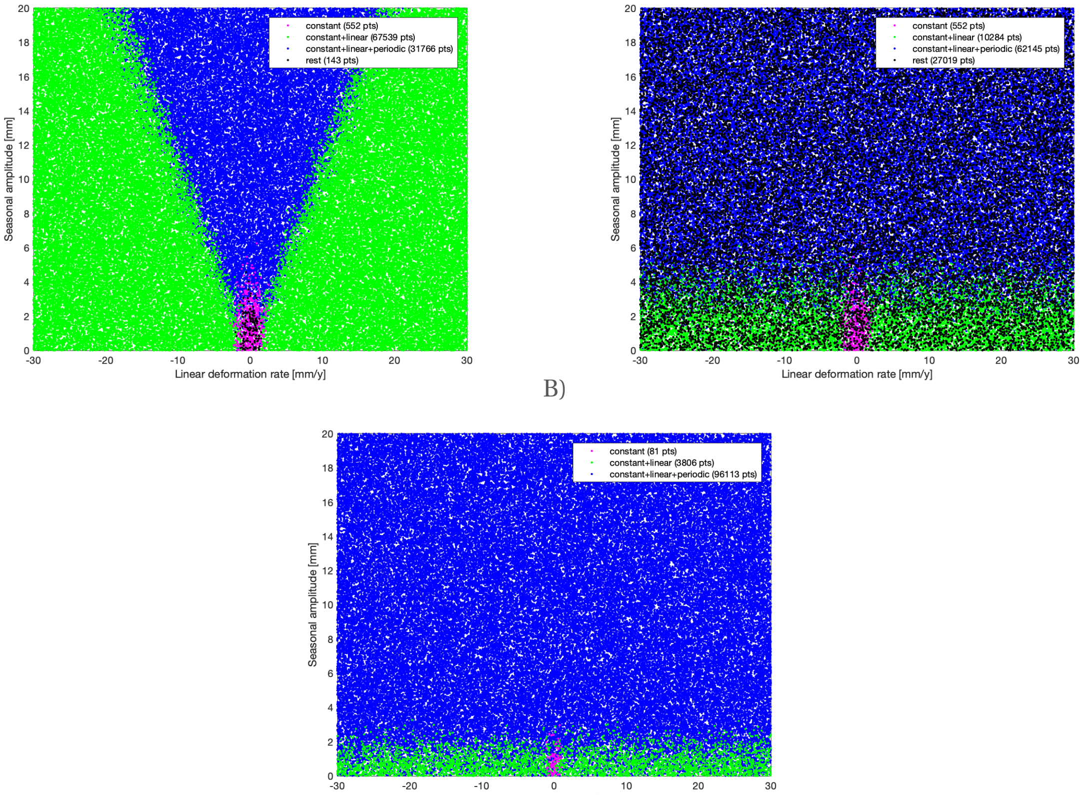

A)

B)

C)

Figure 5.3: Alternative hypothesis testing with the constant model as base (H0). A) Model extension method. B) Sequential OMT method. C) Minimal OMT method.

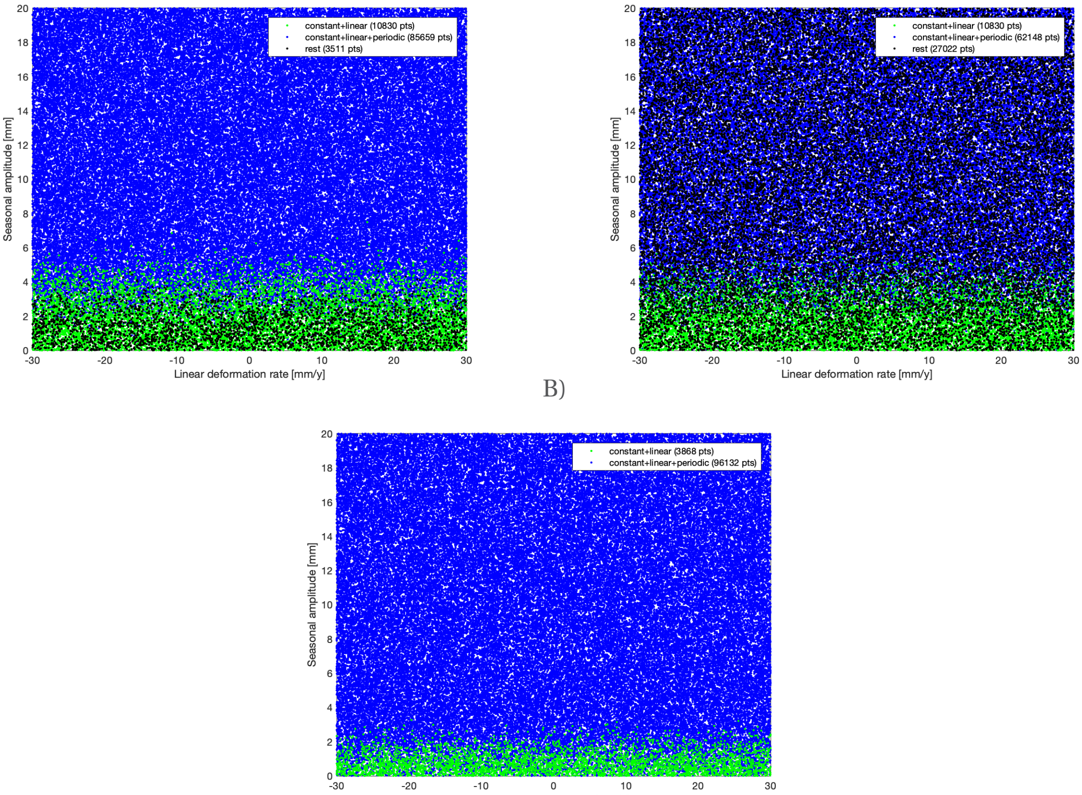

A)

B)

C)

Figure 5.4: Alternative hypothesis testing with the linear model as base (H0). A) Model extension method. B) Sequential OMT method. C) Minimal OMT method.

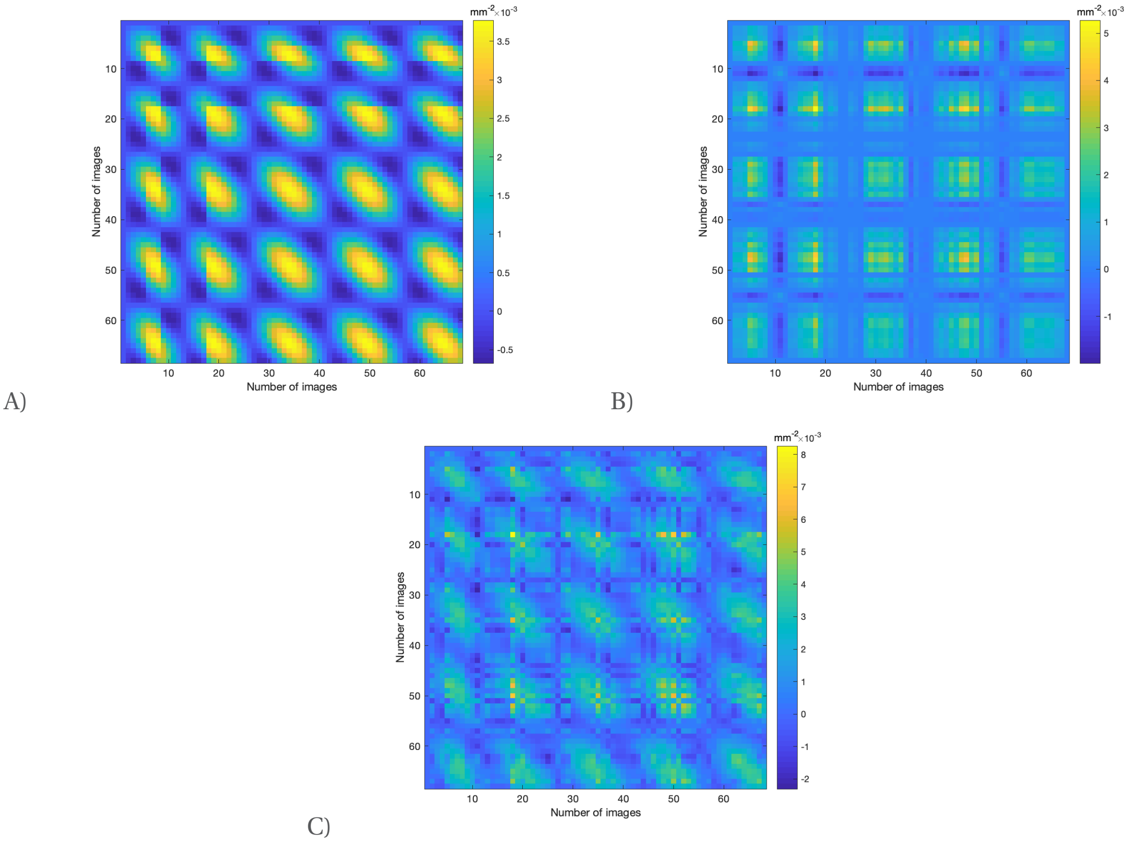

Figure 5.5: Examples of the so-called L_j-matrix for different models. A) Linear+periodic model. B) Linear+temperature model. C) Linear+periodic+temperature model.

model, as manifested itself before.

Using the developed framework to test a library of alternative hypothesis, the range of models can easily be extended. It should be noted that for the Model extension approach, all models should be an extension of H_0. For the OMT based methods, this restriction does not apply. To show the performance of the approaches with an increased amount of models, the constant+linear+temperature and the constant+linear+-periodic+temperature model are added. Because of seasonal variation of the temperature, the temperature-based model is correlated with the periodic model. However, it still shows a distinguishable signal in time. This can be seen in Fig. 5.5, where the so-called L_j-matrix (see Eq. (5.11)) is shown for the linear+periodic, linear+temperature, and linear+periodic+temperature model. The results of the classification using the three different approaches is shown in Fig. 5.6. The same simulated time series are used as in the tests presented earlier. Hence, no temperature-related signal is simulated, only a linear deformation rate plus a periodic signal with a frequency of one year. The results show that in case of the Model extension method, only in a limited amount of cases a model including temperature is selected (3417 of 100000 simulated time series). However, in case of the OMT-based approaches, this number is much larger. In case of the Minimal OMT approach, a model including temperature is selected in 34989 of the 100000 cases. Hence, despite applying the B-method of testing to account for the change in the degree of freedom of the test, the addition of a single parameter (temperature) in the model influences the classification result significantly. This effect is much less in case of the Model extension method. The results based on the simulated data show that each of the three methods have their advantages and disadvantages. The Model extension approach only enables the use of H_j which are an extension of H_0, and the approach does not perform properly in case the constant model is chosen as the null-hypothesis. The Sequential OMT approach, as presented here, has the disadvantage that many time series remain unclassified. The Minimal OMT approach appears to be most sensitive to selection of the model with the most parameters, hence over-fitting. In the trade-off for the selection of the most appropriate approach, also the objective of the testing procedure should be considered. For some of

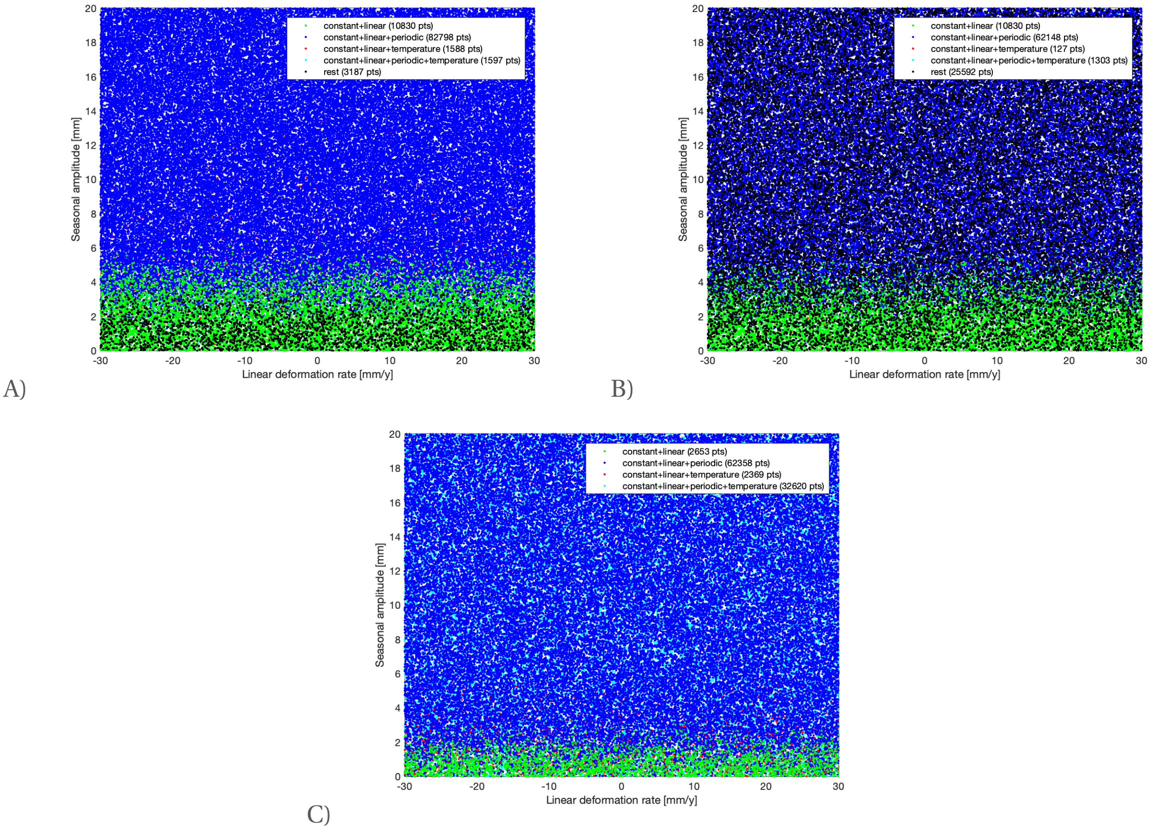

Figure 5.6: Alternative hypothesis testing with the linear model as base (H0) and the inclusion of the temperature model. A) Model extension method. B) Sequential OMT method. C) Minimal OMT method.

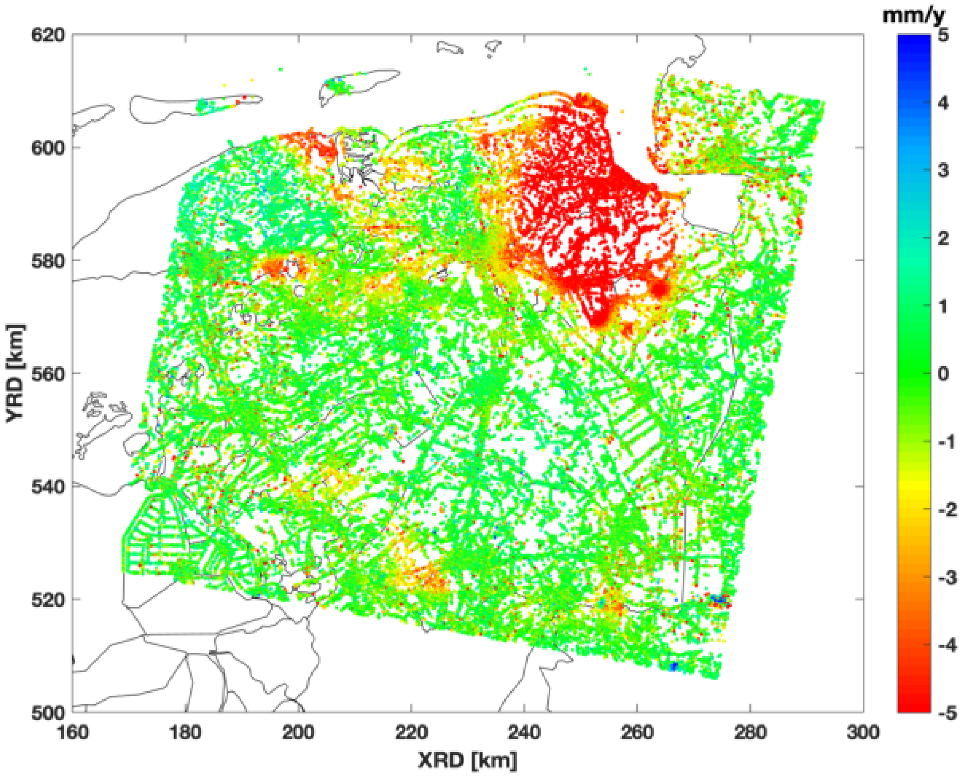

Figure 5.7: Linear velocity rates [mm/y] in Groningen, The Netherlands, based on a RadarSAT-2 dataset of 98 images acquired between September 2009 and November 2016.

the applications mentioned in Section 5.2 the *best* fitting model is desired, whereas in other cases a certain model should only be adopted when the improvement is *significant*. An example of the latter is the detection of jumps in the time series. Only if the jump is significant, the corresponding model should be selected. With the objective of a classification of scatterers for further interpretation and integration of the data, the selection of the best model is desirable. As this is the main objective in this study, the Minimal OMT approach is adopted here for application to real data of the Groningen area.

5.4.2. GRONINGEN AREA

To illustrate the application of the Minimal OMT approach to real data, a PSI dataset is used based on RadarSAT-2 data covering Groningen, The Netherlands. The dataset contains 98 images, acquired between September 2009 and November 2016. In total 371891 PS have been detected. The resulting linear deformation rates are shown in Fig. 5.7. The result of the Minimal OMT approach using the constant, constant+linear and constant+linear+periodic model is visualized in Fig. 5.8. As indicated in Section 5.4.1, the use of the constant model as individual hypothesis should be considered with care, due to the uncertainty in the spatial reference applied. The stochastic model used for all the approaches is based on a variogram model which is estimated based on a ’constant’ area within the dataset, see Chapter 4. Hence, the stochastic model is assumed to describe the measurement and residual atmospheric noise in the data reasonably well.

The results show that for most PS the constant+linear+periodic model is selected. Hence, most time series show a significant periodic effect. The spatial distribution of the classified PS shows that no PS with a constant behavior are found in the main gas extraction region in Groningen.

As it can be argued that the use of a constant model as a separate hypothesis is not desirable, Fig. 5.9 shows the classification with the constant+linear and constant+linear+periodic models only. The spatial distribution of both classes is rather homogeneous. This suggests that the occurrence of a periodic signal in the deformation time series is mainly dependent on local effects. To illustrate the potential to extent the library of alternative hypotheses, additional models involving the temperature are added. As is shown in Fig. 5.5,

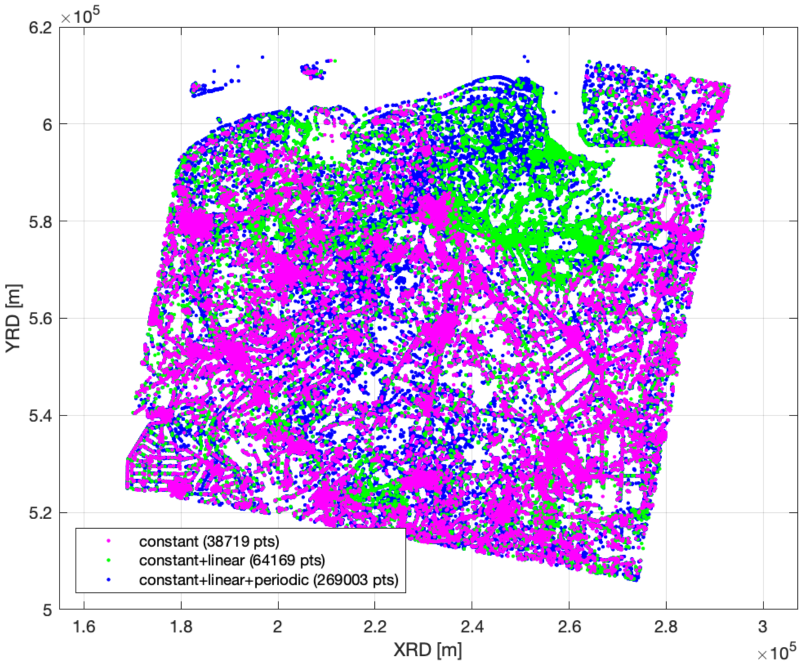

Figure 5.8: MHT result based on the minimal OMT approach using a constant, constant+linear and constant+linear+periodic model. The results show indeed no PS with a constant behavior are detected in the major gas extraction region. Note that the dots are overlapping, and the dots for the constant model are plotted last, and are therefor more prominently visible.

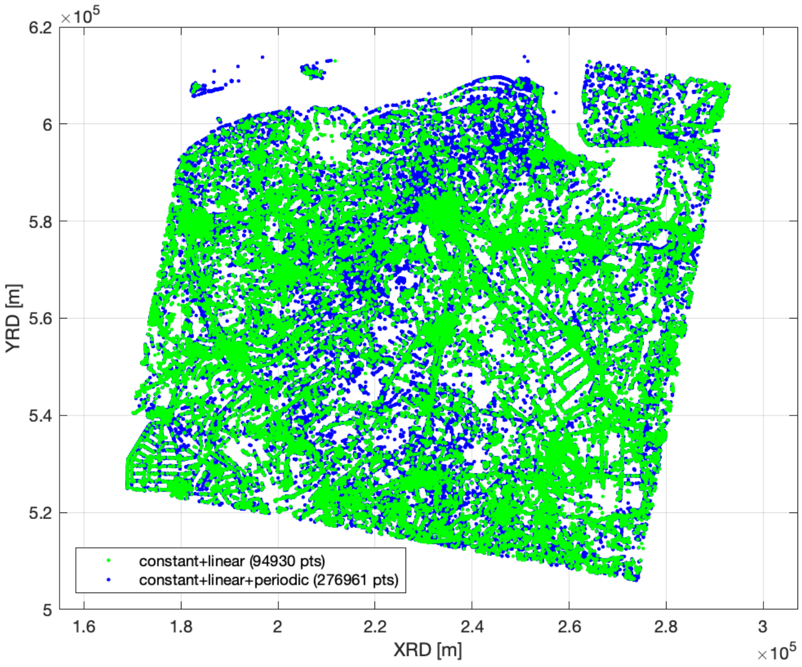

Figure 5.9: MHT result based on the minimal OMT approach using a constant+linear and constant+linear+periodic model.

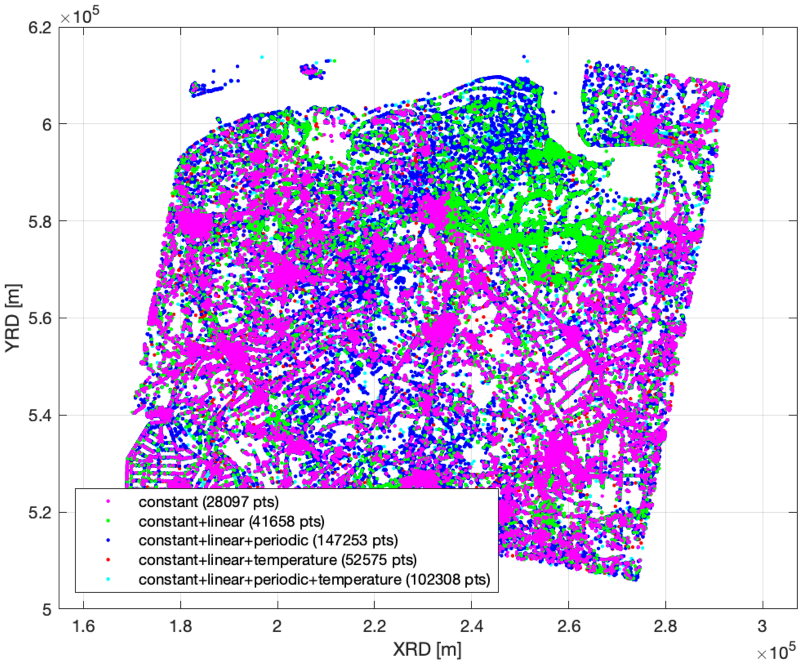

Figure 5.10: MHT result based on the minimal OMT approach using combinations of a constant, linear, periodic and temperature model.

the model including temperature is correlated with the periodic model, but still shows a significant different pattern. The resulting classification is shown in Fig. 5.10. Almost half of the PS appear to have a temperature related signal component in their deformation time series.

5.5. CONCLUSIONS

Multiple Hypothesis Testing (MHT) can be applied to Persistent Scatterer time series with the objective to classify scatterers, to reduce 'leakage' to other parameters or the stochastic model, or to detect anomalies in the time series. Based on the same framework of hypothesis testing, the B-method of testing, and the use of test quotients, different testing approaches can be applied. In this study three approaches have been implemented and evaluated: the Model extension, the Sequential OMT, and the Minimal OMT approach. Application to simulated data shows that each approach has its advantages and disadvantages. The Model extension approach only enables the use of alternative hypothesis which are an extension of the null hypothesis. The Sequential OMT approach, in its current implementation, has the disadvantage that many time series remain unclassified. The Minimal OMT approach appears to be most sensitive to selection of the model with the most parameters, leading to over-fitting. In the trade-off for the selection of the most appropriate approach, also the objective of the testing procedure should be considered. For some of the applications mentioned the *best* fitting model is desired, whereas in other cases a certain model should only be adopted when the improvement is *significant*. An example of the latter is the detection of jumps in the time series. Only if the jump is significant, the corresponding model should be selected. With the objective of a classification of scatterers for further interpretation of the data, the selection of the best model is desirable. As this is the main objective in this study, the Minimal OMT approach was adopted for application to real data of the Groningen area, The Netherlands. With the current implementation of the testing framework, the library of alternative hypothesis can easily be extended and evaluated efficiently for millions of PS time series.

Although the current implementation provides satisfying results, it is recommended to implement and test a fourth testing strategy: the parameter significance test (Teunissen, 2000, Teunissen et al., 2005). In this case, the most extended functional model is applied to all PS time series. Subsequently, the *significance* of each parameter is tested. For each PS, only the significant parameters are maintained in the final functional model.

Next step in the research will be to investigate how the classification results can be used for further interpretation of the PS dataset. One of the objectives hereby is the separation of different deformation regimes. Whether this can be based on the time series classification results only, or should be based on an integrated analysis with other (derived) data, needs to be investigated.

6

STANDARDIZED DATA FORMAT

6.1. INTRODUCTION

InSAR is one of the geodetic techniques providing data for ground motion analysis. A standardized data format for InSAR data is desirable. Such a standardized data format would aid the development of analysis software, would increase the interchangeability of the software used, would make the user less dependent on a particular InSAR data supplier, and would make the exchange of data with other parties easier.

A standardized data format should fulfill a number of requirements. In general, the format should be easy to use, be supported by standard software packages, usable on long-term, and efficient in storage and use. It would be an advantage if the data format is self-contained, that is, all information is stored in a single file. Regarding InSAR data, an additional requirement is that the data format can be used both for the original InSAR datasets, potentially consisting of millions of points and hundreds of epochs, and for reduced datasets.

Here, a standardized data format for InSAR is presented. The format is based on the earlier developments within the CUPiDO software package (Van Leijen et al., 2017a,b). The CUPiDO tool set aims at integration of geodetic data for ground motion analysis. In the current version of CUPiDO, the integration of levelling and GNSS data is enabled. Here, we present both the concept of a CUPiDO compatible data format for InSAR, and the integration concept of InSAR in the CUPiDO tool.

6.2. DATA FORMAT CONCEPT

The standardized data format for InSAR data is based on the space-time matrix concept, see Fig. 6.1. Hereby, the InSAR observations are stored as a matrix of m points and n epochs. In case of InSAR, the matrix will in general be (almost) full, since for detected coherent scatterers a full time series is obtained. However, the data format also allows for the inclusion of temporary coherent scatterers. In that case, the matrix will show some sparsity. This capability of the use of sparse matrices also enables the application of the space-time matrix for other techniques in the future, for instance levelling, where the distribution of observations will be more scattered. The space-time matrix concept can be extended to a space-time array, with d data layers. For example, the three North-East-Up components of GNSS measurements can be stored, or the intensities of the radar scatterers in case of InSAR observations. The space-time array is accompanied by point related information. Part of this information is mandatory, such as point ID, coordinates, and in case of InSAR measurements the sensitivity in North-East-Up direction. In additional, optional contextual information can be added, such as information on soil type, ground water level or building foundation for each individual point. Similarly, obligatory and optional information regarding the epochs should or can be added. The acquisition date and time are obligatory fields. In addition, time dependent variables can be added as contextual information, such as weather related parameters. In all cases holds that the attributes and formatting of the variables applied should be consistent with the datasets of the different techniques. Hereby, integration of the data using the CUPiDO tool set, making use of corresponding points and epochs, is possible.

The final part of the dataset is formed by the meta data. The meta data contains general information about the dataset (satellite mission, track), data types used, and possible information about pre-processing steps applied to the data. Furthermore, the stochastic model describing the data is provided, see Chapter 4.

All data is stored efficiently in NetCDF format. Both original InSAR datasets, and reduced datasets, which

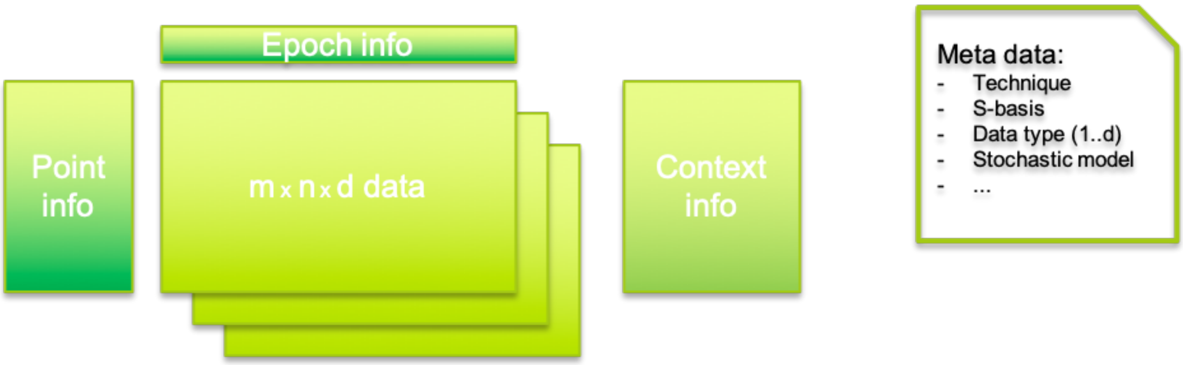

Figure 6.1: Illustration of the space-time matrix data concept. The observations are stored in an *mxnxd* data array. This array is accompanied by point specific, epoch specific, and contextual information. All data and information is stored in a single NetCDF file. This includes the Meta-data, describing the specifics of the dataset.

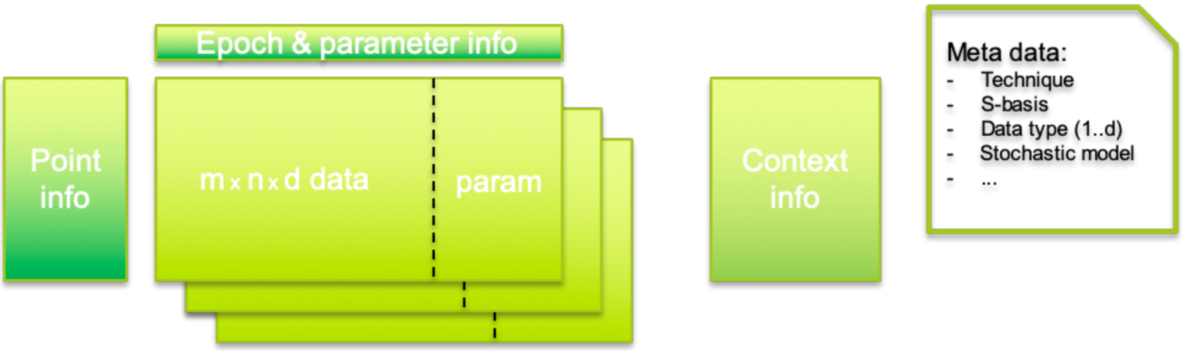

Figure 6.2: The space-time matrix concept, using the NetCDF file format, enables an efficient extension of the stored data, e.g. by estimated parameters estimated based on the observations.

are most suitable for integration with other types of observations via the CUPiDO tool, can be stored using the same setup. For each dataset (satellite mission, ascending or descending orbit, track) a separate NetCDF file is created.

The size of the space-time array is flexible. This means that additional parameters can be added to the array, see Fig. 6.2. For example, in case of InSAR, derived parameters can be added, such as linear deformation rate, height above terrain level, and in case of reduced datasets, the number of points used in the data reduction. The InSAR data is stored in *undifferenced*[1] format. This means that the references of the dataset, both in time and space, are maintained in the dataset. This could mean that one row and one column in the space-time matrix contain zeros. Alternative, for example the mean in time and or space could be used as reference. In any case, the number of rows and columns in the space-time matrix equals the number of points and epochs involved. Storing the data in undifferenced format enables efficient matrix operations to derive other representations, such as single- and double-differences, see Fig. 6.3. In addition, the undifferenced format enables easy application of S-transformations, that is, the change of the references, see Fig. 6.4. These S-transformations can potentially be combined with subset operations on the space-time matrix, both in space and time.

6.3. INTEGRATION IN CUPIDO

InSAR data in the proposed standardized NetCDF data format enables the integration of INSAR in the CUPiDO tool set. The most likely approach is to create a compressed dataset first, since a) this reduces the computational burden, and b) it enables the data reduction to the benchmark locations of the other techniques

---

[1] Note that in the InSAR community the undifferenced format is often annotated as a double-difference format. However, this is strictly not correct. In fact, in double-difference format the matrix would contain $m-1$ rows and $n-1$ columns.

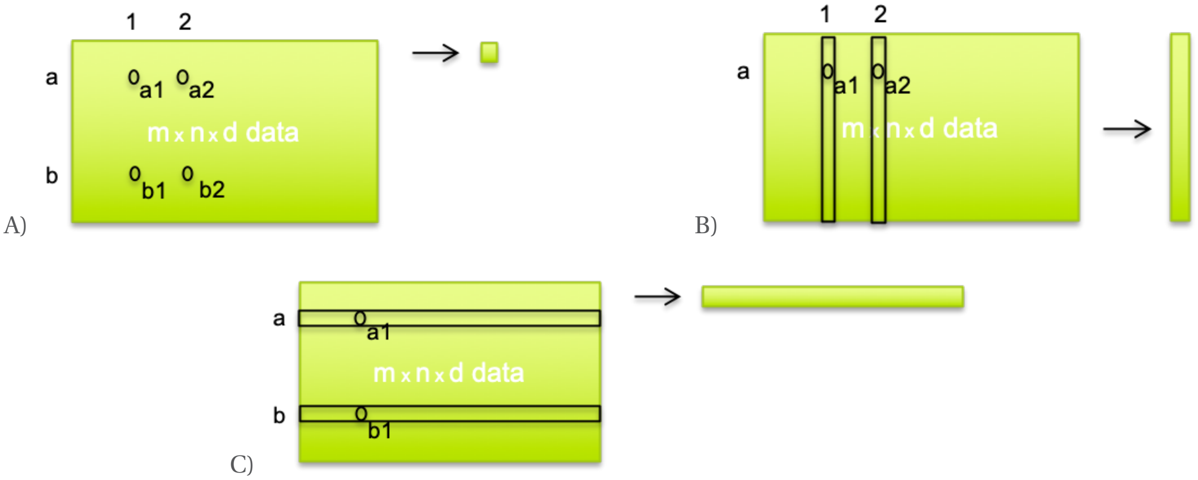

Figure 6.3: Illustration of the efficient operations possible on the space-time matrix. A) The construction of a single double-difference based on four observations. B) The construction of the relative displacement between two epochs. C) The construction of the relative displacement time series between two points.

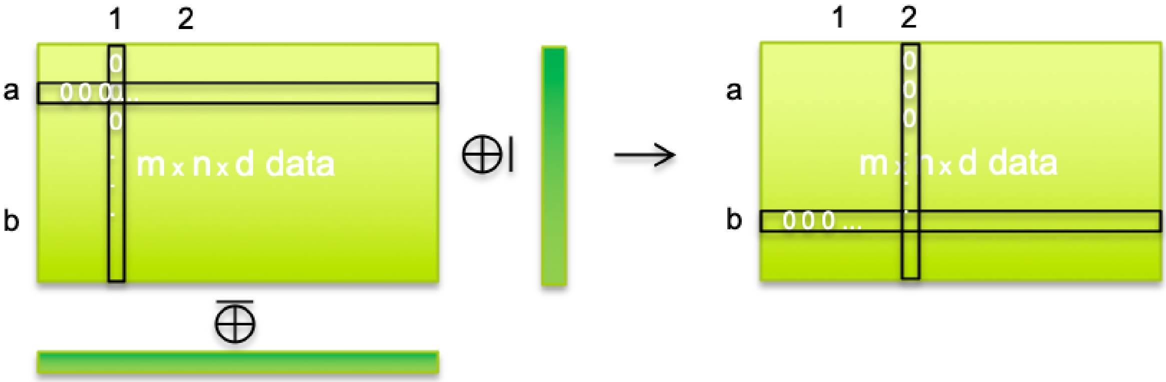

Figure 6.4: Illustration of the application of S-transformations on the space-time matrix. By applying efficient matrix operations, the the spatial and temporal references can easily be adapted.

(levelling, GNSS), to optimize the integration potential of the CUPiDO algorithm. Different data compression techniques can be applied, see Section 3.2. As mentioned, a compression of the data to the benchmark locations is the most obvious choice for the data integration in CUPiDO. However, a reduction to a (quadtree) grid and linking of grid cells to benchmark locations is also possible. In the time domain, the InSAR time series can be compressed to at least the epochs of the levelling and GNSS campaign data, with possible subsampling of the data in the remaining time gaps.

Each InSAR dataset will be inserted in CUPiDO as a separate NetCDF dataset. Due to the sensitivity vectors provided for each data point, the relation to the leveling (vertical) and GNSS (3D) observations is provided. Once inserted in CUPiDO, the corresponding benchmarks and epochs between the different datasets (between levelling, GNSS, and the various InSAR datasets) can be established. The existing starting points in the CUPiDO algorithm are maintained (Van Leijen et al., 2017b):

1. The number of from-points and from-epochs is minimized.
2. No cross-double-differences are formed. Hence, the double differences are formed per technique and directional component. This means that in case of InSAR double-differences are formed per dataset.

Based on the space-time matrix structure of the InSAR data, the double-differences per dataset can easily be constructed. Here, also the error propagation is applied to the stochastic model supplied (see Chapter 4) to generate the covariance matrix corresponding to the double-difference InSAR observations generated by CUPiDO.

6.4. CONCLUSIONS

In this chapter a standard data format is presented for InSAR data. The data format is based on the space-time matrix concept. This concept enables the storage of InSAR observations, point and epoch related data, contextual data and meta data in a consistent framework, that can potentially also be applied to observations by other measurement techniques. The data is stored efficiently per dataset in a single NetCDF file. This setup enables a straightforward integration of InSAR data in the CUPiDO framework for data integration.

7

CONCLUSIONS

In the introduction of this report, two main areas of improvement have been defined for the stochastic modelling of InSAR data:

1. Handling large data dimensions: a computationally efficient method is required that results in a full covariance matrix in which off-diagonal elements are not neglected.
2. Minimization of potential biases in the stochastic model due to choices made on the functional model (e.g., modeling InSAR time as a linear deformation rate).

This study has resulted in a pragmatic approach to obtain an InSAR stochastic model that can handle large data dimensions, and reduces the effect of functional modeling. It is achieved by calculation of the stochastic parameters per InSAR stack, in an area that is assumed not to be affected by surface deformation, and is sufficiently large to be representative for modeling residual atmospheric effects. To further reduce the effect of the functional model, spatio-temporal variograms are estimated after removal of a linear rate and a periodic signal. To compute the covariance matrix in an efficient way, stochastic parameters are estimated from the spatio-temporal variograms. Propagation of full covariance matrices when using a reduced dataset in space and time is avoided, using the derived analytical functions to compute the elements of the covariance matrix as function of the number of deformation estimates over which averaging takes place in space and time. This way, a computationally efficient approximation of the exact covariance matrix is obtained.

Different data reduction techniques can be applied to generate a spatially reduced dataset, such as a the use of a regular grid, a quadtree decomposition, clustering techniques such as K-means, and a reduction to existing benchmark locations. The latter is especially relevant regarding the integration with other geodetic techniques, such as levelling and Global Navigation Satellite Systems (GNSS). For all techniques holds that the mean operator should be used to calculate the representative value per grid cell, cluster or benchmark location, based on the original scatterers involved, to enable the application of the stochastic model for reduced datasets presented.

A standardized InSAR data format is proposed, that can be used both for original InSAR datasets of individual scatterers, as well as for reduced datasets. The data format is based on the space-time matrix concept, that enables the storage of InSAR observations in undifferenced format, together with information on points and epochs. Apart from the minimal required information, such as point coordinates and measurements dates, contextual information can be added, for improved interpretation. All data, including meta data describing the dataset and the stochastic model, are stored efficiently in a single NetCDF format.

To reduce potential biases in the stochastic model due to choices in the functional model, two studies are performed. In the first, the added value of the use of Numerical Weather Models (NWM) to mitigate the atmospheric signal delay is investigated. The analysis shows that no significant improvement, and even a slight deterioration, of the variability in the PS deformation time series is obtained when using a NWM. This is mainly caused by the error induced by the difference in timing between the NWM output generation and the SAR acquisition. This timing eror has two causes: 1) the standardized output times of generic NWM realizations, and 2) the uncertainty in the NWM model parameters (e.g., wind speed and direction), affecting the distribution of the water vapor predictions. This particularly applies to the turbulent part of the tropospheric signal delay. In more mountainous areas compared to the Netherlands, where the stratification effect of the atmosphere is more dominant, application of NWM has shown to have a more positive effect.

To optimize the fit of the functional models applied to the InSAR time series, three alternative approaches of Multiple Hypothesis Testing (MHT) have been implemented and evaluated. All approaches are based on the concepts of the B-method of testing and the use of test quotients, to enable the comparison of tests with different degrees of freedom. Application shows that different results are obtained for each method. The choice of the most suitable method is dependent on the question whether the *best* or an *acceptable* model is desired. In case of the clustering of scatterers as input to study different deformation regimes, the Mimimal OMT approach is selected and demonstrated.

Summarizing, the study ‘Improving the Functional and Stochastic Model of InSAR’ has delivered a pragmatic method for the computation of a full covariance matrix for (reduced) InSAR datasets, ready to be able to discriminate the deformation model(s) that best fit the geodetic data, and to integrate geodetic techniques (leveling, GNSS, InSAR) in the computation of subsidence signals.

BIBLIOGRAPHY

Agram, P. S. and Simons, M. (2015). A noise model for insar time series. *Journal of Geophysical Research: Solid Earth*, 120(4):2752–2771.

Baarda, W. (1968). *A testing procedure for use in geodetic networks*, volume 5 of *Publications on Geodesy*. Netherlands Geodetic Commission, Delft, 2 edition.

Baarda, W. (1976). Reliability and precision of networks. In *VIIth International Course for Engineering Surveys of high precision*, pages 1–11, Darmstadt, Germany.

Bekaert, D., Walters, R., Wright, T., Hooper, A., and Parker, D. (2015). Statistical comparison of insar tropospheric correction techniques. *Remote Sensing of Environment*, 170:40 – 47.

Brcic, R., Parizzi, A., Eineder, M., Bamler, R., and Meyer, F. (2010). Estimation and compensation of ionospheric delay for sar interferometry. In *International Geoscience and Remote Sensing Symposium, Honolulu, Hawaii, USA, 25–30 July 2010*, pages 2908–2911.

Bruna, M. F. D. (2020). Analyzing subsidence in the Netherlands with attribute-enriched InSAR data. Master's thesis, Delft University of Technology, Delft, the Netherlands.

Chang, L. and Hanssen, R. F. (2015). A probabilistic approach to InSAR time series post-processing. *IEEE Transactions on Geoscience and Remote Sensing*, 54(1):421–430.

Cressie, N. and Hawkins, D. M. (1980). Robust estimation of the variogram. *Journal of the International Association for Mathematical Geology*, 12(2):115–125.

de Heus, H. M., Joosten, P., Martens, M. H. F., and Verhoef, H. M. E. (1994). Geodetische deformatie analyse: 1d- deformatieanalyse uit waterpasnetwerken. Technical Report 5, Delft University of Technology, LGR Series, Delft.

Dheenathayalan, P. (2019). *Optimizing the exploitation of persistent scatterers in satellite radar interferometry*. PhD thesis, Delft University of Technology, Delft, the Netherlands.

Ferretti, A., Prati, C., and Rocca, F. (2001). Permanent scatterers in SAR interferometry. *IEEE Transactions on Geoscience and Remote Sensing*, 39(1):8–20.

Genton, M. G. (1998). Highly robust variogram estimation. *Mathematical Geology*, 30(2):213–221.

Gomba, G., Parizzi, A., De Zan, F., Eineder, M., and Bamler, R. (2016). Toward operational compensation of ionospheric effects in SAR interferograms: The split-spectrum method. *IEEE Transactions on Geoscience and Remote Sensing*, 54(3):1446–1461.

Hanssen, R. F. (2001). *Radar Interferometry: Data Interpretation and Error Analysis*. Kluwer Academic Publishers, Dordrecht.

Kampes, B. M. (2006). *Radar Interferometry: Persistent Scatterer Technique*. Springer, Dordrecht, The Netherlands.

Ketelaar, V. B. H. (2009). *Satellite Radar Interferometry: Subsidence Monitoring Techniques*. Springer, Dordrecht, The Netherlands.

Lindenbergh, R. and Hanssen, R. (2003). Eolian deformation detection and modeling using airborne laser altimetry. In *International Geoscience and Remote Sensing Symposium, Toulouse, France, 21–25 July 2003*, pages cdrom, 4 pages.

Liu, S. (2012). *Satellite Radar Interferometry: estimation of atmosphere delay*. PhD thesis, Delft University of Technology, Delft, the Netherlands.

NAM (2017). Ensemble Based Subsidence application to the Ameland gas field – long term subsidence study part two (LTS-II) continued study. Technical report, NAM, Assen, Netherlands.

Neyman, J. and Pearson, E. S. (1933). On the problem of the most efficient tests of statistical hypotheses. *Philosophic Transactions of the Royal Society London, Series A*, 231:289–337.

Perissin, D. (2006). *SAR super-resolution and characterization of urban targets*. PhD thesis, Politecnico di Milano, Italy.

Samiei-Esfahany, S. (2017). *Exploitation of Distributed Scatterers in Synthetic Aperture Radar Interferometry*. PhD thesis, Delft University of Technology, Delft, the Netherlands.

Samiei-Esfahany, S. and Bähr, H. (2015). Research and development project for geodetic deformation monitoring, for long-term study on anomalous time-dependent subsidence in the Wadden sea region. Technical report, Nederlandse Aardolie Maatschappij B.V., Assen, Netherlands. EP201505216980.

Teunissen, P. (2017). Distributional theory for the dia method. *Journal of Geodesy*, pages 1–22.

Teunissen, P. J. G. (1990). Quality control in integrated navigation systems. *IEEE Aerospace and Electronic Systems Magazine*, 5(7):35–41.

Teunissen, P. J. G. (2000). *Testing theory; an introduction*. Delft University Press, Delft, 1 edition.

Teunissen, P. J. G. (2006). *Network quality control*. VSSD, Delft, 1 edition.

Teunissen, P. J. G., Simons, D. G., and Tiberius, C. C. J. M. (2005). *Probability and observation theory*. Delft Institute of Earth Observation and Space Systems (DEOS), Delft University of Technology, The Netherlands.

Teunissen, P. J. G., Zaminpardaz, S., and Tiberius, C. C. J. M. (2020). On the integrity of deformation monitoring. *Geomatics, Natural Hazards and Risk*, 11(1):399–413.

Tiberius, C. (1998). *Recursive data processing for kinematic GPS surveying*. PhD thesis, Delft University of Technology, Delft, the Netherlands.

van de Kerkhof, B., Pankratius, V., Chang, L., van Swol, R., and Hanssen, R. (2018). Automatic insar phase modeling and quality assessment using machine learning and hypothesis testing. In Moreno, J., editor, *IGARSS 2018 - 2018 IEEE International Geoscience and Remote Sensing Symposium*, volume 2018, pages 4427–4430, United States. IEEE.

van De Kerkhof, B., Pankratius, V., Chang, L., Van Swol, R., and Hanssen, R. (2020). Individual scatterer model learning for satellite interferometry. *IEEE Transactions on Geoscience and Remote Sensing*, 58(2):1273–1280.

van der Marel, H. (2020). Comparison of GNSS processing methodologies for subsidence monitoring, project report for NAM. Technical report, Delft University of Technology, Delft, Netherlands.

Van Leijen, F., Samiei-Esfahany, S., Van der Marel, H., and Hanssen, R. (2017a). A standardized approach for the integration of geodetic data for deformation analysis. In *2017 IEEE International Geoscience and Remote Sensing Symposium: International Cooperation for Global Awareness, IGARSS 2017 - Proceedings*, volume 2017-July, pages 957–960, United States. Institute of Electrical and Electronics Engineers (IEEE).

Van Leijen, F., Samiei-Esfahany, S., Van der Marel, H., and Hanssen, R. (2017b). Uniformization of geodetic data for deformation analysis; contribution to the research project: Second phase of the long-term subsidence study in the Wadden Sea region (LTS2). Technical report, Delft University of Technology, Delft, Netherlands.

van Leijen, F. J. (2014). *Persistent Scatterer Interferometry based on geodetic estimation theory*. NCG, Amersfoort, The Netherlands.

Yu, C., Li, Z., Penna, N. T., and Crippa, P. (2018). Generic atmospheric correction model for interferometric synthetic aperture radar observations. *Journal of Geophysical Research: Solid Earth*, 123(10):9202–9222.

Yu, C., Penna, N. T., and Li, Z. (2017). Generation of real-time mode high-resolution water vapor fields from GPS observations. *Journal of Geophysical Research: Atmospheres*, 122(3):2008–2025.

Zaminpardaz, S. and Teunissen, P. (2018). Dia-datasnooping and identifiability. *Journal of Geodesy*, pages 1–17.

A

DERIVATIONS

Derivation of equation 4.6

For an averaging cell with m number of PSs each with deformation y_i, the deformation vector and its covariance matrix is written as

$$y = \begin{bmatrix} y_1 \\ y_2 \\ \vdots \\ y_m \end{bmatrix}, \quad Q_y = \begin{bmatrix} \sigma^2 & \sigma_{12} & \sigma_{13} & \dots & \sigma_{1m} \\ \sigma_{12} & \sigma^2 & \sigma_{23} & \dots & \sigma_{2m} \\ \vdots & \vdots & \vdots & \ddots & \vdots \\ \sigma_{1m} & \sigma_{2m} & \sigma_{3m} & \dots & \sigma^2 \end{bmatrix}, \tag{A.1}$$

Now, the deformation of the assumed averaging cell z is computed as

$$z = \begin{bmatrix} \frac{1}{m} & \frac{1}{m} & \dots & \frac{1}{m} \end{bmatrix} \begin{bmatrix} y_1 \\ y_2 \\ \vdots \\ y_m \end{bmatrix}. \tag{A.2}$$

Based on the linear covariance propagation rule, the variance of z is computed as

$$\sigma_z^2 = \begin{bmatrix} \frac{1}{m} & \frac{1}{m} & \dots & \frac{1}{m} \end{bmatrix} \begin{bmatrix} \sigma^2 & \sigma_{12} & \sigma_{13} & \dots & \sigma_{1m} \\ \sigma_{12} & \sigma^2 & \sigma_{23} & \dots & \sigma_{2m} \\ \vdots & \vdots & \vdots & \ddots & \vdots \\ \sigma_{1m} & \sigma_{2m} & \sigma_{3m} & \dots & \sigma^2 \end{bmatrix} \begin{bmatrix} \frac{1}{m} \\ \frac{1}{m} \\ \vdots \\ \frac{1}{m} \end{bmatrix} = \frac{1}{m^2} \sum_{i=1}^{m} \sum_{j=1}^{m} \sigma_{ij}. \tag{A.3}$$

The right hand side of the above equation can be written as

$$\sigma_z^2 = \frac{1}{m^2} \sum_{i=1}^{m} \sum_{j=1}^{m} \sigma_{ij} = \frac{1}{m^2} \left(\sum_{i=1}^{m} \sigma^2 + 2 \sum_{i=1}^{m} \sum_{j=i+1}^{m} \sigma_{ij} \right). \tag{A.4}$$

Note that the average of all the off-diagonal elements of Q_y is:

$$\bar{s} = \frac{2}{m(m-1)} \sum_{i=1}^{m} \sum_{j=i+1}^{m} \sigma_{ij}. \tag{A.5}$$

So the second component of the right hand side of equation A.4 can be written as

$$2 \sum_{i=1}^{m} \sum_{j=i+1}^{m} \sigma_{ij} = m(m-1)\bar{s}. \tag{A.6}$$

Inserting equation A.6 in equation A.4, we have:

$$\boxed{\sigma_z^2 = \frac{1}{m^2} \left(m\sigma^2 + m(m-1)\bar{s} \right) = \frac{\sigma^2 + (m-1)\bar{s}}{m}.} \tag{A.7}$$

Derivation of equation 4.8

The value of two averaging cells z_1 and z_2 is written as

$$\underbrace{\begin{bmatrix} z_1 \\ z_2 \end{bmatrix}}_{z} = \underbrace{\begin{bmatrix} \frac{1}{m_1} & \frac{1}{m_1} & \dots & \frac{1}{m_1} & 0 & 0 & \dots & 0 \\ 0 & 0 & \dots & 0 & \frac{1}{m_2} & \frac{1}{m_2} & \dots & \frac{1}{m_2} \end{bmatrix}}_{A} \underbrace{\begin{bmatrix} y_{1,1} \\ y_{1,2} \\ \vdots \\ y_{1,m_1} \\ y_{2,1} \\ y_{2,2} \\ \vdots \\ y_{2,m_2} \end{bmatrix}}_{y}. \tag{A.8}$$

The covariance matrix of vector $[z_1, z_2]^T$ is then (using linear covariance propagation rule):

$$Q_z = \begin{bmatrix} \sigma^2_{z_1} & \sigma_{z_1 z_2} \\ \sigma_{z_1 z_2} & \sigma^2_{z_2} \end{bmatrix} = A \begin{bmatrix} Q_{y_1} & Q_{y_1 y_2} \\ Q^T_{y_1 y_2} & Q_{y_2} \end{bmatrix} A^T, \tag{A.9}$$

where the matrix $Q_{y_1 y_2}$ is the cross-covariance between the points of the two cells:

$$Q_{y_1 y_2} = \begin{bmatrix} c_{11} & c_{12} & \dots & c_{1m_2} \\ \vdots & \vdots & \ddots & \vdots \\ c_{m_1 1} & c_{m_2 2} & \dots & c_{m_1 m_2} \end{bmatrix}. \tag{A.10}$$

The component $\sigma_{z_1 z_2}$ can then be written as

$$\boxed{\sigma_{z_1 z_2} = \bar{c} = \frac{1}{m_1 m_2} \sum_{i=1}^{m_1} \sum_{j=1}^{m_2} c_{ij}.} \tag{A.11}$$

Derivation of equations of table 4.4 (for the nugget effect)

For the nugget effect, there is no spatial or temporal correlation and so the values of $\text{cov}\{Z^{T_p}_{G_i}, Z^{T_q}_{G_j}\}$ is zero when $G_i \neq G_j$ or when $T_p \neq T_q$. For the case of $G_i = G_j$ and $T_p = T_q$, the value $Z^{T_p}_{G_i}$ is computed as the average among m_i number of points in space and n_p epochs in time (i.e., in total $M = m_i n_p$ independent samples). So, based on the error propagation rule (for independent samples), the variance of $Z^{T_p}_{G_i}$ is computed as

$$\boxed{\mathrm{D}\{Z^{T_p}_{G_i}\} = \frac{\sigma^2_0}{M}.} \tag{A.12}$$

Derivation of equations of table 4.4 (for the spatially correlated component)

For the spatially correlated component, there is no correlation in the time domain. so the values of $\mathrm{cov}\{Z_{G_i}^{T_p}, Z_{G_j}^{T_q}\}$ is zero when $T_p \neq T_q$ (provided that there is no overlap between the temporal averaging intervals T_p and T_q). The value of $Z_{G_i}^{T_p}$ is computed as

$$z = \begin{bmatrix} \frac{1}{n_p} & \frac{1}{n_p} & \cdots & \frac{1}{n_p} \end{bmatrix} \begin{bmatrix} z_1 \\ z_2 \\ \vdots \\ z_{n_p} \end{bmatrix}, \tag{A.13}$$

where $z_1 \ldots z_{n_p}$ are the spatially averaged cells for the epochs within the temporally averaged interval T_p: $t_1, t_2, \ldots, t_{n_p}$. There is no correlation between z_i components, and the variance of each z_i component is derived from equation 4.6 as

$$\sigma_{z_i}^2 = \frac{\sigma^2 + (m_i - 1)\bar{s}}{m_i}, \quad \text{for } i = 1, 2, \ldots, n_p. \tag{A.14}$$

Based on the linear error propagation rule, the variance of $Z_{G_i}^{T_p}$ is computed as

$$\mathrm{D}\{Z_{G_i}^{T_p}\} = \frac{\sigma_s^2 + (m_i - 1)\bar{s}}{m_i n_p}. \tag{A.15}$$

Assuming $\bar{s} = C_s(\bar{h}_i)$ (based on the approximation 4.10), we can write:

$$\boxed{\mathrm{D}\{Z_{G_i}^{T_p}\} = \frac{\sigma_s^2 + (m_i - 1)\bar{s}}{m_i n_p} = \frac{\sigma_s^2}{M} + \frac{m_i - 1}{M} C_s(\bar{h}_i).} \tag{A.16}$$

Furthermore, the covariance between $Z_{G_i}^{T_p}$ and $Z_{G_j}^{T_p}$ can be computed based on equation 4.8 as

$$\mathrm{cov}\{Z_{G_i}^{T_p}, Z_{G_j}^{T_p}\} = \frac{1}{n_p n_p} \sum_{k=1}^{n_p} \sum_{l=1}^{n_p} c_{kl}, \tag{A.17}$$

where c_{kl} are the elements of the cross-covariance between the spatially averaged cells Z_{G_i} and Z_{G_j} at different epochs within the averaging interval T_p:

$$\begin{bmatrix} c_{11} & c_{12} & \cdots & c_{1m_2} \\ \vdots & \vdots & \ddots & \vdots \\ c_{m_1 1} & c_{m_2 2} & \cdots & c_{m_1 m_2} \end{bmatrix} = \begin{bmatrix} \bar{c} & & \\ & \ddots & \\ & & \bar{c} \end{bmatrix}. \tag{A.18}$$

Note that this matrix is diagonal as there is no correlation in the time domain, and the covariances between two averaged cells Z_{G_i} and Z_{G_j} at each epoch is computed based on equation 4.8 as $\bar{c}$. Now, based on the two previous equations, we have:

$$\mathrm{cov}\{Z_{G_i}^{T_p}, Z_{G_j}^{T_p}\} = \frac{1}{n_p n_p} \sum_{k=1}^{n_p} \sum_{l=1}^{n_p} c_{kl} = \frac{1}{n_p n_p} n_p \bar{c} = \frac{\bar{c}}{n_p}. \tag{A.19}$$

Assuming $\bar{c} = C_s(L_{ij})$ where L_{ij} is the distance between the centers of the cells G_i and G_j (based on the approximations 4.10 and 4.15), we can write:

$$\boxed{\mathrm{cov}\{Z_{G_i}^{T_p}, Z_{G_j}^{T_p}\} = \frac{C_s(L_{ij})}{n_p}.} \tag{A.20}$$

Derivation of equations of table 4.4 (for the temporally correlated component)

For the temporally correlated component, there is no correlation in space domain. so the values of $\mathrm{cov}\{Z_{G_i}^{T_p}, Z_{G_j}^{T_q}\}$ is zero when $G_i \neq G_j$ (provided that there is no overlap between the spatial averaging cells G_i and G_j). The value of $Z_{G_i}^{T_p}$ is computed as

$$z = \begin{bmatrix} \frac{1}{m_i} & \frac{1}{m_i} & \dots & \frac{1}{m_i} \end{bmatrix} \begin{bmatrix} z_1 \\ z_2 \\ \vdots \\ z_{m_i} \end{bmatrix}, \tag{A.21}$$

where $z_1 \dots z_{n_p}$ are the temporally averaged values for the PS poits within the spatially averaged cell G_i: $p_1, p_2, \dots, p_{m_i}$. There is no correlation between z_i values and the variance of each z_i is derived from equation 4.6 as

$$\sigma_{z_i}^2 = \frac{\sigma^2 + (n_p - 1)\bar{s}}{n_p}, \quad \text{for } i = 1, 2, \dots, m_i. \tag{A.22}$$

Based on the linear error propagation rule, the variance of $Z_{G_i}^{T_p}$ is computed as

$$\mathrm{D}\{Z_{G_i}^{T_p}\} = \frac{\sigma_s^2 + (n_p - 1)\bar{s}}{n_p m_i}. \tag{A.23}$$

Assuming $\bar{s} = C_t(\Delta \bar{T}_p)$ (based on the approximation 4.10), we can write:

$$\boxed{\mathrm{D}\{Z_{G_i}^{T_p}\} = \frac{\sigma_t^2 + (n_p - 1)\bar{s}}{n_p m_i} = \frac{\sigma_s^2}{M} + \frac{n_p - 1}{M} C_t(\Delta \bar{T}_p).} \tag{A.24}$$

Furthermore, the covariance between $Z_{G_i}^{T_p}$ and $Z_{G_i}^{T_q}$ can be computed based on equation 4.8 as

$$\mathrm{cov}\{Z_{G_i}^{T_p}, Z_{G_i}^{T_q}\} = \frac{1}{m_i m_i} \sum_{k=1}^{m_i} \sum_{l=1}^{m_i} c_{kl}, \tag{A.25}$$

where c_{kl} are the elements of the cross-covariance between the temporally averaged epochs Z^{T_p} and Z^{T_q} at different PS within the spatially averaging cell G_i:

$$\begin{bmatrix} c_{11} & c_{12} & \dots & c_{1m_2} \\ \vdots & \vdots & \ddots & \vdots \\ c_{m_1 1} & c_{m_2 2} & \dots & c_{m_1 m_2} \end{bmatrix} = \begin{bmatrix} \bar{c} & & \\ & \ddots & \\ & & \bar{c} \end{bmatrix}. \tag{A.26}$$

Note that this matrix is diagonal as there is no correlation in the space domain, and the covariances between two averaged intervals Z^{T_p} and Z_{T_q} at each PS is computed based on equation 4.8 as $\bar{c}$. Now, based on the two previous equations, we have:

$$\mathrm{cov}\{Z_{G_i}^{T_p}, Z_{G_i}^{T_q}\} = \frac{1}{m_i m_i} \sum_{k=1}^{m_i} \sum_{l=1}^{m_i} c_{kl} = \frac{1}{m_i m_i} m_i \bar{c} = \frac{\bar{c}}{m_i}. \tag{A.27}$$

Assuming $\bar{c} = C_t(\Delta T_{pq})$ where ΔT_{pq} is the time difference between the centers of the averaging intervals T_p and T_1 (based on the approximations 4.10 and 4.15), we can write:

$$\boxed{\mathrm{cov}\{Z_{G_i}^{T_p}, Z_{G_i}^{T_q}\} = \frac{C_t(\Delta T_{pq})}{m_i}.} \tag{A.28}$$